University of Stuttgart
Faculty of Aerospace Engineering and Geodesy

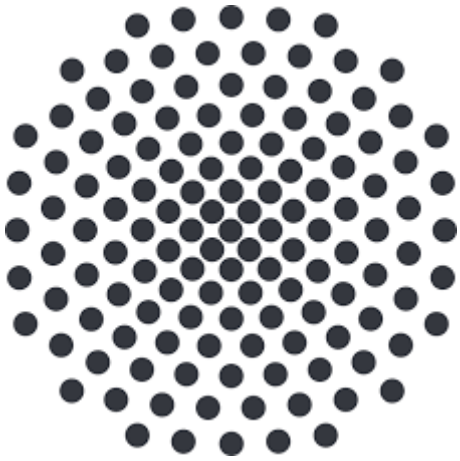

Master's thesis

CFD- Simulation of Icing on a Flying- Wing UAV

Submitted by Michael Henzler
Stuttgart/ Trondheim, April 2024

Norwegian University of Science and Technology
UAV Icing Lab
Department of Engineering Cybernetics

Supervisor: Dr. Richard Hann
M.Sc. Markus Lindner

University of Stuttgart
Institute of Aerodynamics and Gas Dynamics

Supervisor: Dr.-Ing. Thorsten Lutz

Eidesstattliche Erklärung

Hiermit versichere ich, die vorliegende Abschlussarbeit selbstständig und nur unter Verwendung der von mir angegebenen Quellen und Hilfsmittel verfasst zu haben. Sowohl inhaltlich als auch wörtlich entnommene Inhalte wurden als solche kenntlich gemacht. Die Arbeit hat in dieser oder vergleichbarer Form noch keinem anderem Prüfungsgremium vorgelegen.

Datum: 16.04.2024 Unterschrift: M. Henzler

Abstract

Unmanned Aerial Vehicles (UAVs) are experiencing rapid market growth due to their numerous military and commercial applications. However, atmospheric icing is a critical challenge, potentially leading to significant losses in aerodynamic performance and stability. This study investigates ice accretion on the Skywalker X8, a low-cost, fixed-wing UAV with a high payload ratio. Generally, fixed-wing UAVs have advantages over rotary-wing UAVs due to their operational efficiency advantages. The first objective of this work is to create a precise 3D CAD model of the Skywalker X8, which is suitable for computational fluid dynamics simulations, as no 3D model was available. Additionally, the airfoil of this UAV was unknown and is derived from the CAD model, which is used for multishot ice accretion simulations. They are conducted using the FENSAP-ICE software to predict 3D ice shapes in glaze, mixed, and rime ice icing conditions. The iced geometries obtained from the simulations will then be used to evaluate the aerodynamic performance degradation compared to the clean airfoil in terms of lift, drag, and pitching moment coefficients. Furthermore, the calculated ice shapes will be compared to digitized ice shapes resulting from icing wind tunnel tests to validate the simulation results. Since there are no measured wind tunnels available for the Skywalker X8 airfoil, the performance simulation setup and the grid convergency study were performed using the comparable S5010 airfoil for which wind tunnel data are available.

Kurzfassung

UAVs erfahren aufgrund ihrer zahlreichen militärischen und kommerziellen Anwendungen ein schnelles Marktwachstum. Die atmosphärische Vereisung stellt jedoch eine kritische Herausforderung dar, die zu erheblichen Einbußen bei der aerodynamischen Leistungsfähigkeit und Stabilität führen kann. Diese Arbeit untersucht die Eisbildung an der Skywalker X8, einer kostengünstigen Starrflügel-Drohne mit hohem Nutzlastverhältnis. Starrflügel -Drohnen haben im Allgemeinen Vorteile gegenüber Drehflügler-Drohnen, da sie mit einem kleineren Schub-Gewicht Verhältnis auskommen. Da bisher kein 3D-Modell verfügbar war, das für Strömungssimulationen geeignet ist, besteht das erste Ziel dieser Arbeit darin, ein präzises 3D-CAD-Modell der Skywalker X8 zu erstellen. Außerdem war das Tragflächenprofil dieser Drohne unbekannt und wird aus dem CAD-Modell abgeleitet. Dieses wird anschließend für Multishot-Vereisungssimulationen verwendet. Die Simulationen werden mit der Software FENSAP-ICE durchgeführt, um 3D-Eisgeometrien bei Klareis-, Raueis- und gemischten Bedingungen vorauszusagen. Die aus den Simulationen gewonnenen vereisten Geometrien werden dann verwendet, um die Einbußen der aerodynamischen Leistungsfähigkeit im Vergleich zum reinen Profil in Bezug auf Auftriebs-, Widerstands- und Nickmomentenkoeffizienten zu bewerten. Darüber hinaus werden die berechneten Eisformen mit digitalisierten Eisformen aus Vereisungs-Windkanalversuchen verglichen, um die Simulationsergebnisse zu validieren. Da für das Profil Skywalker X8 keine gemessenen Windkanaldatem zur Verfügung stehen, wird das numerische Setup für die Strömungssimulation zu Ermittlung der aerodynamischen Leistungsfähigkeit und die Gitterkonvergenzstudie mit dem vergleichbaren Profil S5010 durchgeführt, für das Windkanaldaten verfügbar sind.

Contents

List of Symbols

Symbol	Unit	Desciption
C	-	Constant
C	$\mathrm{J\,kg^{-1}\,K^{-1}}$	Heat capacity
C_D	-	Drag coefficient
c	-	Chord length
c_d	-	Drag coefficient
c_l	-	Lift coefficient
c_m	-	Moment coefficient
C_p	-	Pressure Coefficient
d	m	Diameter
E	J	Energy
f	-	Property
f	$\mathrm{m\,s^{-2}}$	Volume force
Fr	-	Froude number
F_s	-	Safty factor
g	$\mathrm{m\,s^{-2}}$	Gravitational acceleration
GCI	-	Grid convergence index
h	-	Discretization parameter
h	m	Hight
h	$\mathrm{kJ\,kg^{-1}}$	Specific enthalpy
k	$\mathrm{m^2\,s^{-2}}$	Turbulent kinetic energy
K	$\mathrm{s^{-1}}$	Inertial parameter
L	$\mathrm{J\,kg^{-1}}$	Latent heat
l	m	Length
LWC	$\mathrm{kg\,m^{-3}}$	Liquid water content
m	kg	Mass

Symbol	**Unit**	**Desciption**
n	-	Normal vector
p	Pa	Pressure
q	$\mathrm{W\,m^{-2}}$	Heat flux
Q_h	$\mathrm{W\,m^{-2}}$	Convective heat flux
R	$\mathrm{J\,kg^{-1}\,K^{-1}}$	Specific gas constant
r	-	Grid refinement factor
Re	-	Reynolds number
S_r	$\mathrm{J\,m^{-3}\,s^{-1}}$	Radiation
T	K	Temperature
t	s	Time
u^+	-	Dimensionless velocity
u_τ	$\mathrm{m\,s^{-1}}$	Friction velocity
u	$\mathrm{m\,s^{-1}}$	Velocity
v	$\mathrm{m\,s^{-1}}$	Velocity
x	m	Postion, coordinate, direction
y	m	Postion, coordinate, direction, wall distance
α	$^\circ$	Angle of Attack
α	$^\circ$	Volume fraction
β	-	Droplet collection efficieny
δ_{ij}	-	Kronecker-delta
ϵ	-	Emissitivity
ϵ	-	Relative error
κ	-	von Karman constant
μ	$\mathrm{kg\,m^{-1}\,s^{-1}}$	Dynamic viscosity
μ_v	$\mathrm{kg\,m^{-1}\,s^{-1}}$	Second viscosity coefficient

Symbol	**Unit**	**Desciption**
ρ	$\mathrm{kg\,m^{-3}}$	Density
σ	$\mathrm{W\,m^{-2}\,K^{-4}}$	Stefan–Boltzmann constant
τ_{ik}	$\mathrm{kg\,m^{-1}\,s^{-2}}$	Element of shear stress tensor
τ_w	$\mathrm{kg\,m^{-1}\,s^{-2}}$	Wall shear stres

List of Indices

Index	Desciption
∞	Free stream
a	Air
d	Droplet
evap	Evaporation
f	Film
fusion	Fusion
g	Total
i	Component
ice	Ice
j	Component
k	Component
l	Laminar
subl	Sublimation
t	Turbulent
w	Water

List of Abbreviations

Abbreviation	Description
AoA	Angle of attack
BC	Boundary condition
BL	Boundary layer
BSL	Baseline Model
BVLOS	Beyond visual line of sight
CAD	Computer aided design
CFD	Computational fluid dynamics
CFL	Courant–Friedrichs–Lewy
DNS	Direct numerical simulation
FAA	Federal Aviation Administration
GCI	Grid convergence index
IAG	Institut für Aerodynamik und Gasdynamik
IPS	Ice protection system
IWT	Icing wind tunnel
LE	Leading edge
LWC	Liquid water content
MCCS	Maximum combined cross section
MVD	Mean volume diameter
PDE	Partial differential equation
RANS	Reynolds-averaged Navier-Stokes equation
RSM	Reynolds-stress model
SfM	structure-from-Motion
SLD	Superlarge droplets

Abbreviation	**Description**
SST	Shear-Stress Transport
TE	Trailing edge
UAV	Unmanned Aerial Vehicle
URANS	Unsteady Reynolds-averaged Navier-Stokes equation
VLOS	Visual line of sight

List of Figures

List of Tables

1 Motivation

UAVs are an emerging technology with many military and commercial applications. The first UAVs were primarily used and developed for military purposes. They are often related to reconnaissance, combat support, and communication missions. As the technology became widely available, a commercial UAV- market with a variety of new applications was established. Today, they are already used for urgent medical supplies, agriculture, search and rescue, and maintenance missions for energy power lines. Currently, companies are working on future projects like autonomous urban air mobility [1, 2]. Forecasts about the growth rate for the UAV- the market differ in numbers, but the trend is around 10-25 % annually [1]. The Federal Aviation Administration (FAA) provides a more detailed forecast for the US market. The report of 2022 [3] estimates the annual growth rate for model aircraft in the private sector to be around 10 %. The growth rate of commercial small UAVs is estimated to be around 20 % and for remote pilot aircraft around 40 % over the next five years. Comparisons to the FAA forecast of 2020 [4] show that the potential in the UAV- market was underestimated. As the field of applications grows, the UAVs are designed mission specifically. Therefore, they come in all shapes and sizes [2]. Despite numerous advatages,all-weather capable UAVs have to deal with severe weather conditions. One particular weather phenomenon is in flight-atmospheric icing. That can lead to a significant loss in aerodynamic performance and stability [1], which could result in a dangerous crash over populated areas. In the past, research about icing effects on aerial vehicles has focused on conventional commercial aircraft. However, previous studies have shown that various factors cause a significant change in ice accretion compared to crewed transport aircraft. These factors are, for example, the type of aircraft, the size, and the flight speed in terms of typical Mach- and Reynolds numbers [1]. Thus, more research is needed to develop appropriate methods for UAVs. Interesting UAVs to focus on are fixed-wing drones. Due to their higher payload and lower thrust-to-weight ratio, they are often more cost-efficient to operate than rotary-wing UAVs [5]. Therefore, the Skywalker X8 is attractive since it is a low-cost fixed-wing drone with a high payload ratio [6]. It can be used and adapted for various applications, like Arctic research missions, to investigate icing effects on UAVs. One approach is the numerical simulation, which is a cost-efficient method compared to experiments [7]. Thus, this work concentrates on a precise digital 3D reverse-engineering of the Skywalker X8 suitable for Computational fluid dynamics (CFD) simulations. These are performed at a representative 2D- cross-section. Three different temperature cases for glaze, mixed, and rime ice were investigated regarding the geometry of the ice shape and its aerodynamic effect in terms of lift, drag, and pitch moment. The results are compared to IWT test results. Therefore, this research project focuses on the numerical prediction of ice accretion and its aerodynamic effects to develop safe and energy-efficient strategies in icing conditions.

2 Theoretical background

2.1 UAVs

UAVs are defined as pilotless aircraft that are flown without a pilot-in-command on-board and are either remotely and fully controlled from another place or programmed and fully autonomous [8]. Initially, they were developed for armed forces since the beginning of the 1900s and are an essential part of modern defense strategies [2]. Today UAVs have many different applications for military and commercial purposes. Some are already mentioned in chapter 1. One key differentiator in UAV- missions is between the operation within the Visual line of sight (VLOS) and Beyond visual line of sight (BVLOS). Today, most commercial UAV- missions are conducted in VLOS with rotary wing UAVs and limited automation and autonomy because they are easy to operate. Missions in BVLOS are either performed with a remotely piloted or a completely autonomous aircraft. These are often fixed-wing aircraft and need much more automation and control systems to ensure safe operation. UAVs also differ in terms of wingspan, take-off mass, service ceiling, and propulsion system [1].

2.2 Atmospheric Icing

Atmospheric icing relates to meteorological conditions in which supercooled water exists in the atmosphere. Supercooled describes a state of water where the temperature is below the freezing point, but it is still liquid. When the droplets collide with the aircraft, they will freeze on its surface. Supercooled droplets mainly occur in clouds, which is also called in-cloud icing. The droplets in the clouds have an Mean volume diameter (MVD) below 40- 50 microns. Nevertheless, sometimes droplets occur in precipitation. These droplets are characterized by an MVD greater than 40- 50 microns and are, therefore, called Superlarge droplets (SLD). Their trajectory is less deflected by aerodynamic forces because they have a higher inertia. Therefore, SLDs tend to follow a straight-line path and are more likely to collide with surfaces. This is shown in Figure 2.1. SLDs can lead to high ice accretion rates that cover large surface areas. Hence, SLD- icing is considered more severe than in-cloud icing because these conditions can result in significant performance penalties [1, 2]. The shape of the ice geometry is also dependent on the Liquid water content (LWC) and the temperature.

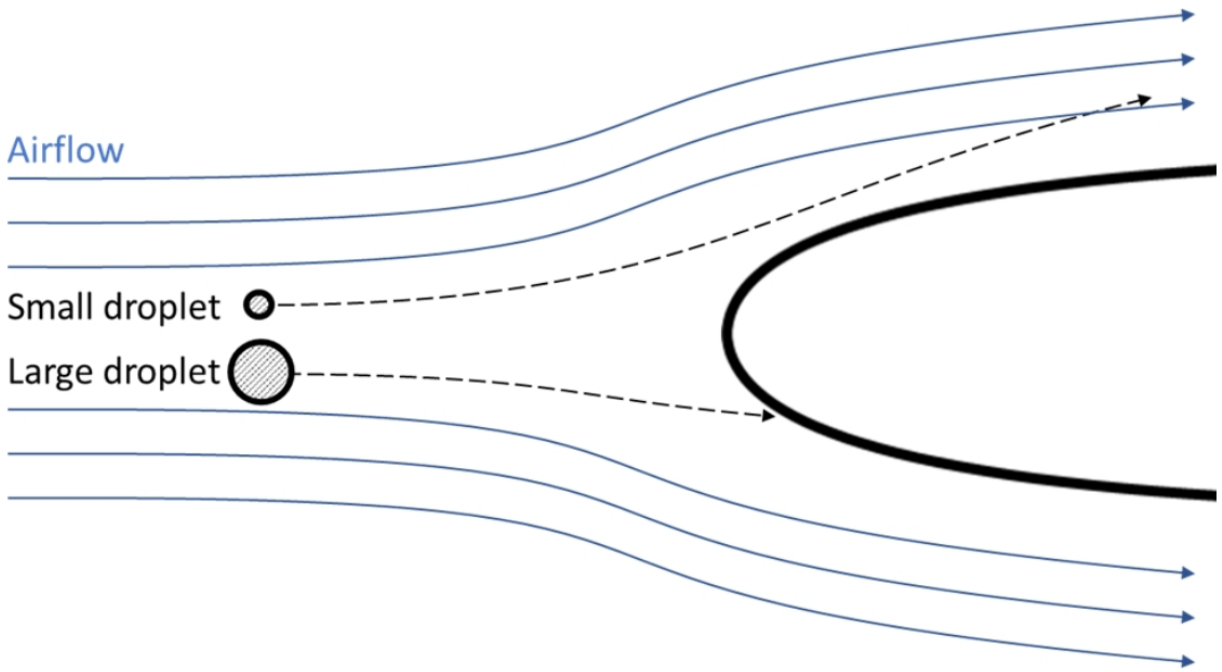

Figure 2.1: Droplet trajectories [2]

2.2.1 Types of Ice

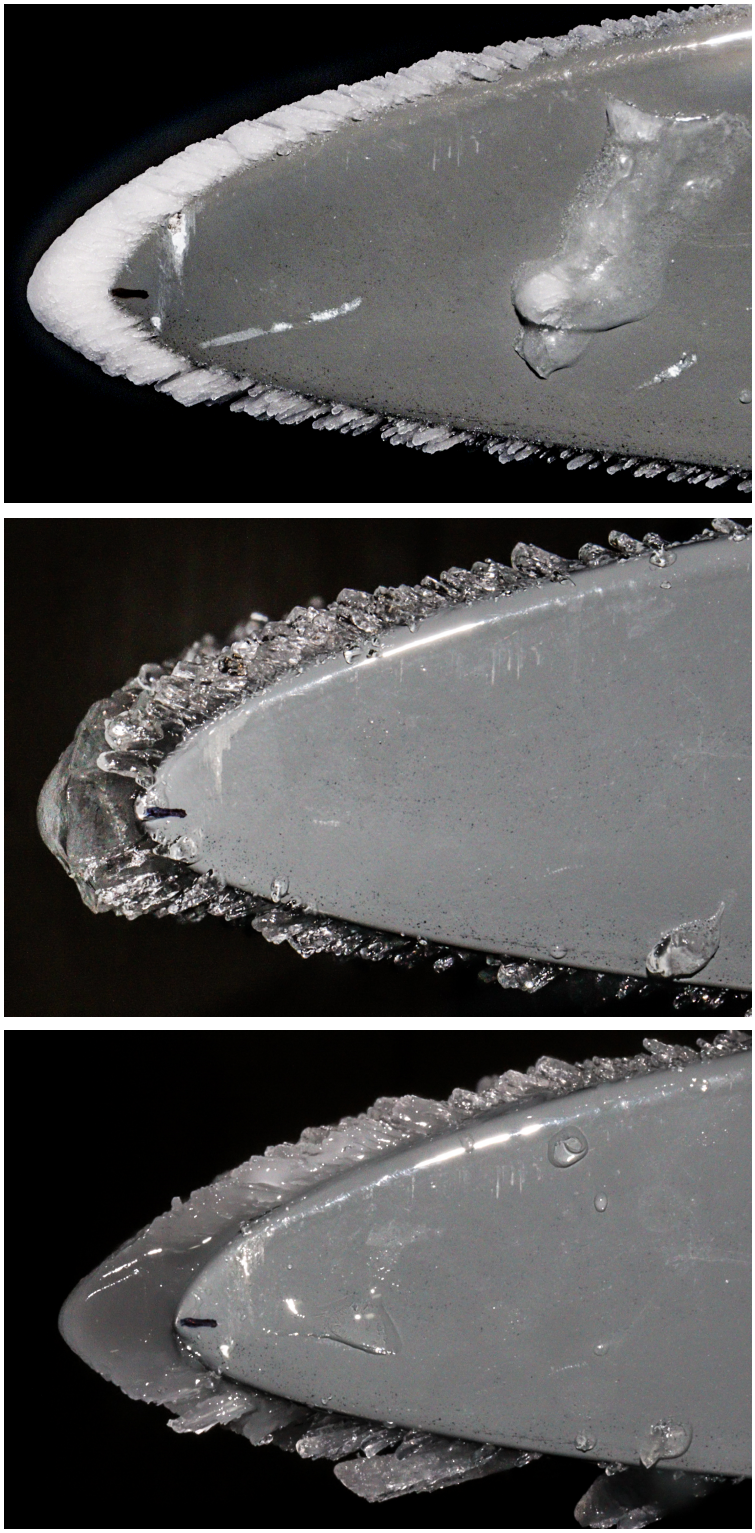

Rime Ice
Rime ice typically occurs at low temperatures. Impinging droplets freeze immediately when impacting cold surfaces. During the ice accretion process, small air pockets are enclosed between the freezing droplets. Rime ice appears white, with small ice feathers forming a rough surface. The shape is typically streamlined and has limited effect on the airfoil's aerodynamics [1, 9].

Glaze Ice
Glaze ice forms at temperatures close to the freezing point. In this temperature regime, the incoming droplets do not freeze instantly at impact on the airframe. This results in a liquid water film gradually freezing on the surface and forming transparent ice shapes. Glaze ice shapes can form very complex geometries that can lead to severe aerodynamic penalties [1, 9].

Mixed Ice
Atmospheric icing often occurs as a combination of glaze and rime ice. Mixed ice is characterized by the partial freezing of impinging droplets and the simultaneous formation of a liquid water film on the surface. These shapes come in many forms that may result in horn-like structures. Ice horns can lead to significant aerodynamic performance losses [1, 9].

Figure 2.2: Ice types [1, 9].

2.2.2 Ice Shapes and their Aerodynamic Effects on Airfoils

Extensive studies involving wind tunnel experiments, in-flight tests, and numerical simulations have revealed that accumulated ice on the leading edge of an aircraft alters the airfoil shape. This results in a loss of aerodynamic performance. Generally, four distinct ice geometries are identified. These ice shapes are schematically illustrated in Figure 2.3 and categorized based on their influence on aerodynamic characteristics [1, 10]

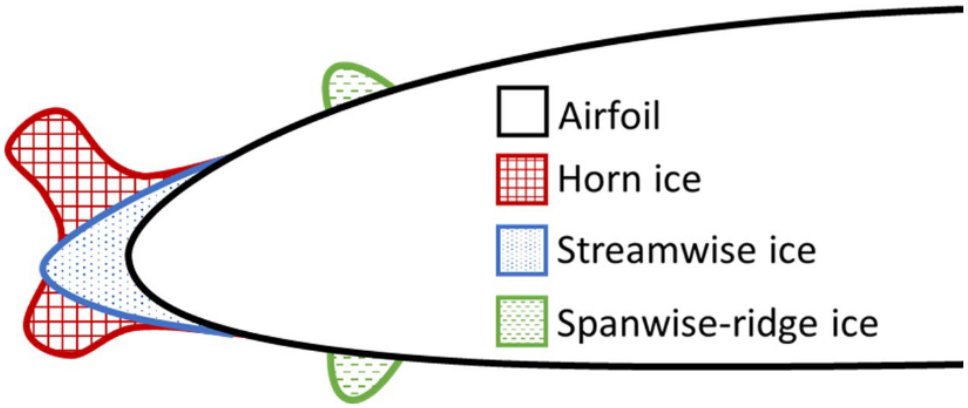

Figure 2.3: In- flight ice shapes [2].

Initially, surface roughness develops before a significant ice shape forms, increasing skin friction drag. This can also trigger early boundary layer transition, leading to early separation and a reduced stall angle [10]. Streamwise ice forms as impinging droplets freeze immediately, impacting the airframe during rime ice conditions. Rime ice is characterized by streamlined shapes with minimal leading-edge separations and flow field disturbances compared to other ice forms like horn ice [1, 10]. However, in glaze ice conditions, horn ice shapes develop, characterized by a separation bubble downstream due to adverse pressure gradients from the discontinuous ice geometry. This bubble alters the wing's pressure distribution, increasing pressure drag and decreasing lift [1, 10]. Additionally, in the combination of SLD icing conditions and an LE Ice protection system (IPS) that does not fully evaporate the water, spanwise-ridge ice can form from refrozen runback water downstream of the protected area. These ridges act as spanwise flow obstacles, significantly impacting aerodynamic performance through early transition and flow separation. Typically, the accumulated ice consists of a mixture of these shapes, disrupting airflow and adversely affecting aircraft stability, control, drag, and lift [1, 10]. The main aerodynamic effects are summarized in Figure 2.3

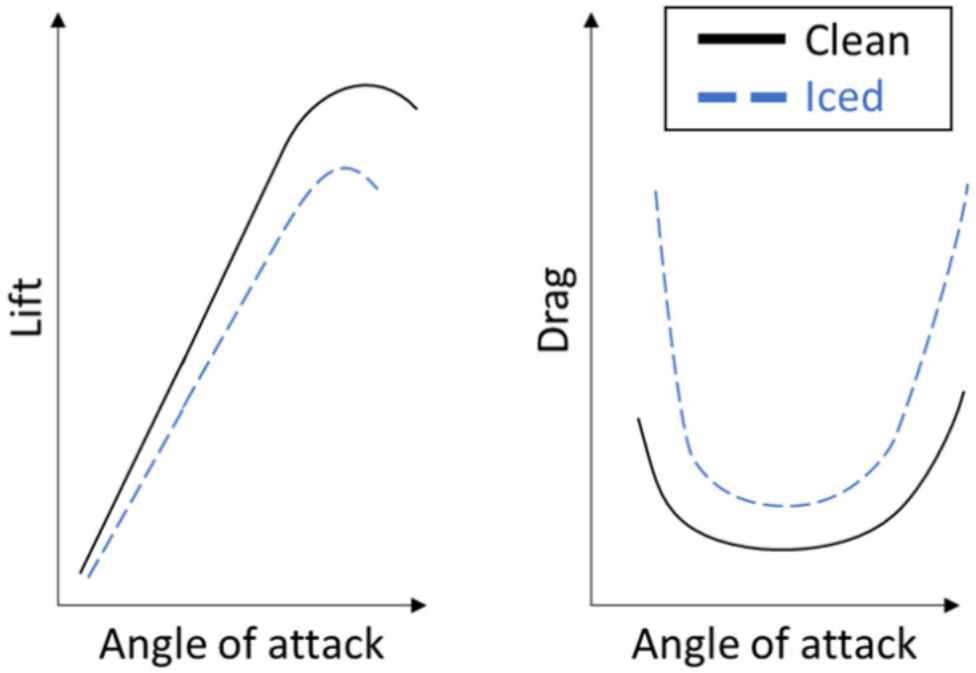

1. Decreased lift
2. Increased drag
3. Altered pitch moments
4. Reduced stall angle
5. Increased mass

Figure 2.4: Aerodynamic effects of icing [1, 9].

2.2.3 Difference to Manned Aerial Vehicles

Several factors contribute to the severity of icing effects on UAVs. Generally, rotary wing UAVs are more vulnerable to icing than fixed-wing UAVs. Smaller UAVs accumulate ice faster than larger aircraft because the aerodynamic forces are smaller and, therefore, displace less air. This causes more droplets to collide with the surfaces. Small UAVs often have external control surface actuators. If they freeze due to runback water, this will result in loss of maneuverability [1, 9]. Regarding the airspeed, UAVs typically operates at lower velocities. Therefore, they cannot benefit from aerodynamic heating and ice shedding based on shear stresses acting on the ice [9]. Additionally, UAVs often operate in laminar flow regimes. Thus, they can take advantage of the lower drag but the flow is more sensitive to flow separation caused by icing-induced disturbances. This will lead to increased aerodynamic penalties [1, 9]. UAVs are often manufactured of polymer-based composite materials, which have a lower thermal conductivity than aluminum alloys. Therefore, the latent heat is less spread, leading to more runback water. This can form more complex ice shapes with larger

aerodynamic penalties [1]. Another issue regarding icing of UAVs is energy since it is a limited resource. Especially battery-powered UAVs have to deal with an optimization between an electro-thermal IPS for de- or anti-icing, increased thrust based on an increased drag, and reduced lift or a path modification [1]. Icing also changes the vehicle's flight performance, stability, and control. Therefore, the flight controller has to be capable of detecting icing conditions and limits the flight envelope if necessary. This becomes even more important since UAVs are expected to operate fully autonomous in the future [1].

2.3 Fundamentals of CFD

CFD is the numerical investigation of three-dimensional flow fields described by the conservation of mass, momentum, and energy. CFD can be efficiently used for research and development, in addition to experiments and analytical methods. The equations are numerically solved in a discrete number of points in the flow region. Therefore, the region and the needed equations are discretized in time and spatial dimensions. [7].

2.3.1 Conservation Equations

As already mentioned above, a flow field is described by a system of coupled partial differential equations, the conservation of mass Equation (2.1), momentum Equation (2.2), and energy Equation (2.3) [11]. Additionally, an equation of state like the ideal gas equation is needed to close the system Equation (2.4) [7]. The equations are shown in cartesian coordinates, tensor notation, and a conservative formulation [11].

$$\frac{\partial \rho}{\partial t} + \frac{\partial}{\partial x_i}\left(\rho u_i\right) = 0 \tag{2.1}$$

$$\frac{\partial}{\partial t}\left(\rho u_i\right) + \frac{\partial}{\partial x_j}\left(\rho u_i u_j\right) - \frac{\partial \tau_{ij}}{\partial x_j} + \frac{\partial p}{\partial x_i} = \rho f_i \tag{2.2}$$

$$\frac{\partial}{\partial t}(\rho E) + \frac{\partial}{\partial x_i}\left(\rho u_i E + u_i p\right) - \frac{\partial}{\partial x_i}\left(u_j \tau_{ji}\right) + \frac{\partial q_i}{\partial x_i} = \rho u_i f_i + S_\mathrm{r} \tag{2.3}$$

$$p = \rho R T \tag{2.4}$$

The Stokes hypothesis Equation (2.5) [12] for Newtonian fluids connects the viscous stress tensor Equation (2.6) with the strain-rate tensor Equation (2.7) [11]. δ_{ij} denotes the Kronecker-delta [7].

$$2\mu + 3\mu_v = 0 \tag{2.5}$$

$$\tau_{ij} = 2\mu S_{ij} - \delta_{ij}\frac{2}{3}\mu\frac{\partial u_k}{\partial x_k} \tag{2.6}$$

$$S_{ij} = \frac{1}{2}\left(\frac{\partial v_i}{\partial x_j} + \frac{\partial v_j}{\partial x_i}\right) \tag{2.7}$$

$$\delta_{ij} = \begin{cases} 1 & \text{für } i = j \\ 0 & \text{für } i \neq j \end{cases} \tag{2.8}$$

2.3.2 Boundary Layer

The Boundary layer (BL) is a thin region near walls where viscous effects dominate the flow [13]. For turbulent flows, the velocity profile is divided into three different regions, which are shown in Figure 2.5. The BL is represented by the dimensionless wall distance y^+ and the dimensionless velocity u^+. They are given by Equation (2.10) and Equation (2.9), respectively [14].

$$u^+ = \frac{\bar{u}}{u_\tau} \quad \text{with} \quad u_\tau = \sqrt{\frac{\tau_W}{\rho}} \tag{2.9}$$

$$y^+ = \frac{u_\tau y}{v} \tag{2.10}$$

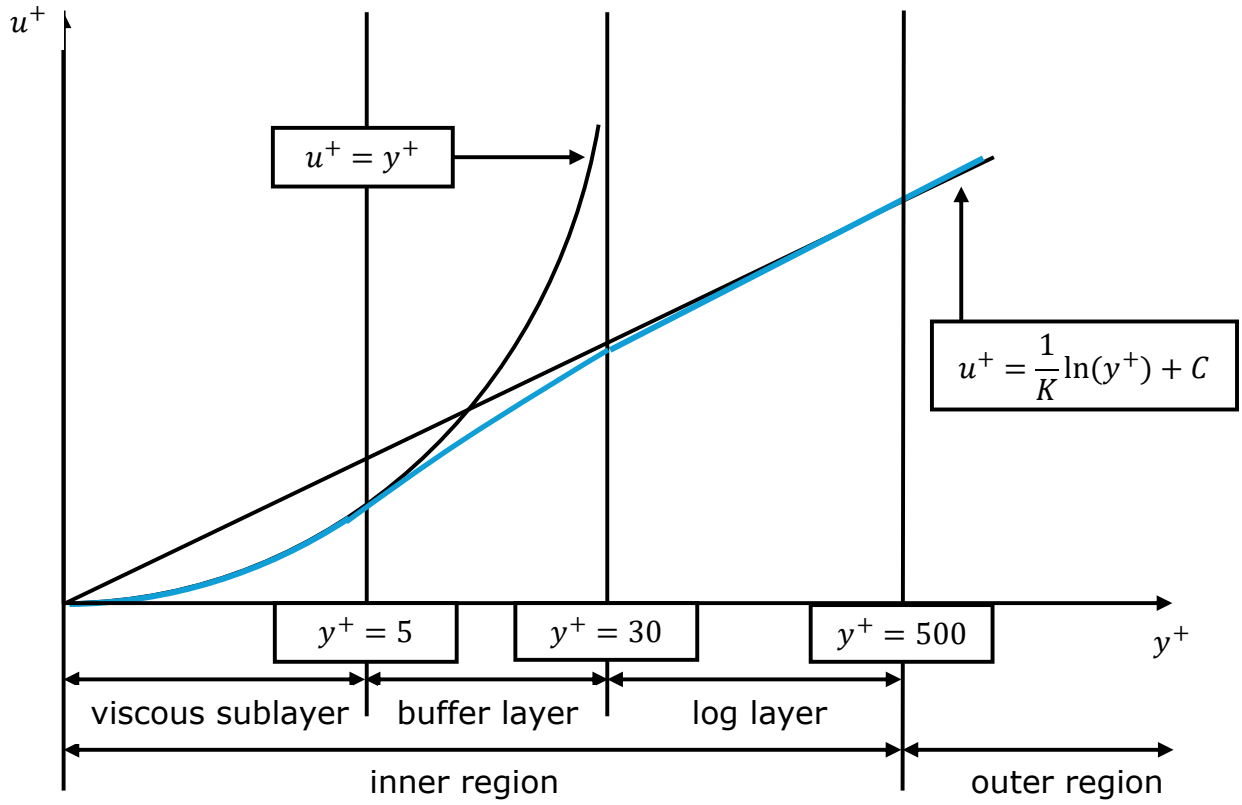

Figure 2.5: Dimensionless boundary layer [15]

Viscous sublayer $y^+ < 5$
In the viscous layer, the fluid is dominated by the viscous effect. Therefore, it can be assumed that the shear stress of fluid is equal to the wall shear stress. The velocity profile is linear, given by Equation (2.11) [14].

$$u^+ = y^+ \tag{2.11}$$

Buffer layer $5 < y^+ < 30$
In the buffer layer, the viscous and turbulent stresses are of similar magnitude. The velocity profile in that region is complex and, therefore, difficult to define [14].

Log law layer $y^+ > 30$
In the logarithmic layer, turbulence stress dominates the flow [14]. The velocity profile follows a logarithmic function, given by Equation (2.12) [7]

$$u^+ = \frac{1}{\kappa} \ln\left(y^+\right) + C \tag{2.12}$$

Modeling of the near wall region

There are two different approaches to calculating the near-wall flow. The first is the High Reynolds approach. It is less accurate but also less computationally demanding. It is based on wall functions and is used with higher y^+- values if the areas close to the wall are not of primary interest, flow separation is only expected at sharp edges, or the computing capacity is limited. The center of the cell closest to the wall has to be in the logarithmic layer [15]. The second method is called Low Reynolds wall treatment. It is used when velocity or temperature profiles are relevant, flow separation is to be predicted, and sufficient computing capacity is available. The calculation point closest to the wall is at $y^+ < 1$. Therefore, significantly more cells are required in the wall area [15]

High- Reynolds wall treatment with wall function [4]]

Low- Reynolds wall treatment [15]

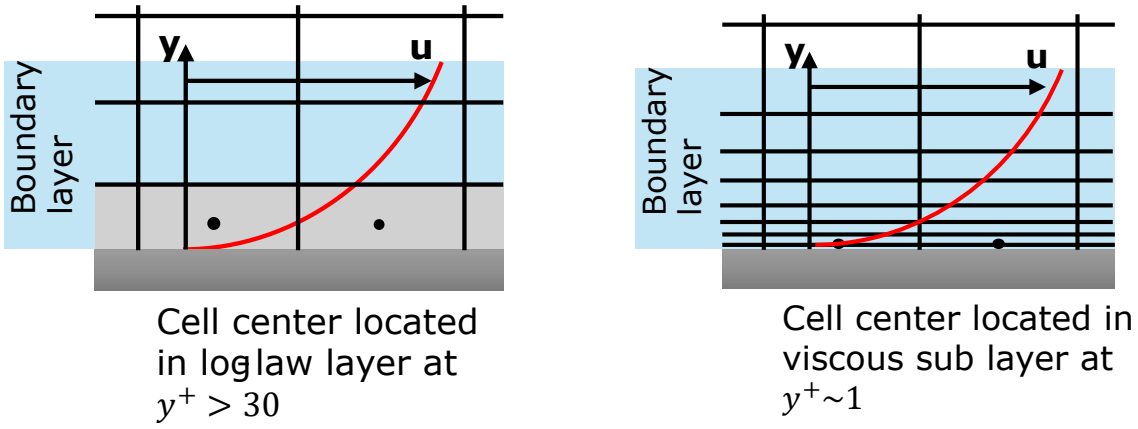

Figure 2.6: Modeling of the near wall region [15]

2.3.3 Turbulence Modeling

Generally, there are two different types of flow. Laminar flow is characterized by fluid particles that flow on layered paths without significant lateral movement perpendicular to the main flow direction. Turbulent flow has stochastically strongly fluctuating vortex structures and thus an unsteady, intensified cross-exchange of all transport variables. The Reynolds number is the dimensionless number that characterizes the flow. In the case of turbulent flows, a high flow resolution is required to capture the smallest vortices [16]. These are created through a cascade process. Large eddies contain the most kinetic energy and will break down into smaller eddies. In the dissipative region, the kinetic energy is transferred into heat. This is shown by Figure 2.7. The kinetic energy is extracted from the mean flow [17]. Solving the differential equations without modeling requires an extremely fine computational mesh to resolve the smallest scales. This method is called Direct numerical simulation (DNS) but leads to high computational effort, which is not useful for industrial applications today. Therefore, different turbulence models were developed to approximate the effects of turbulence. [16].

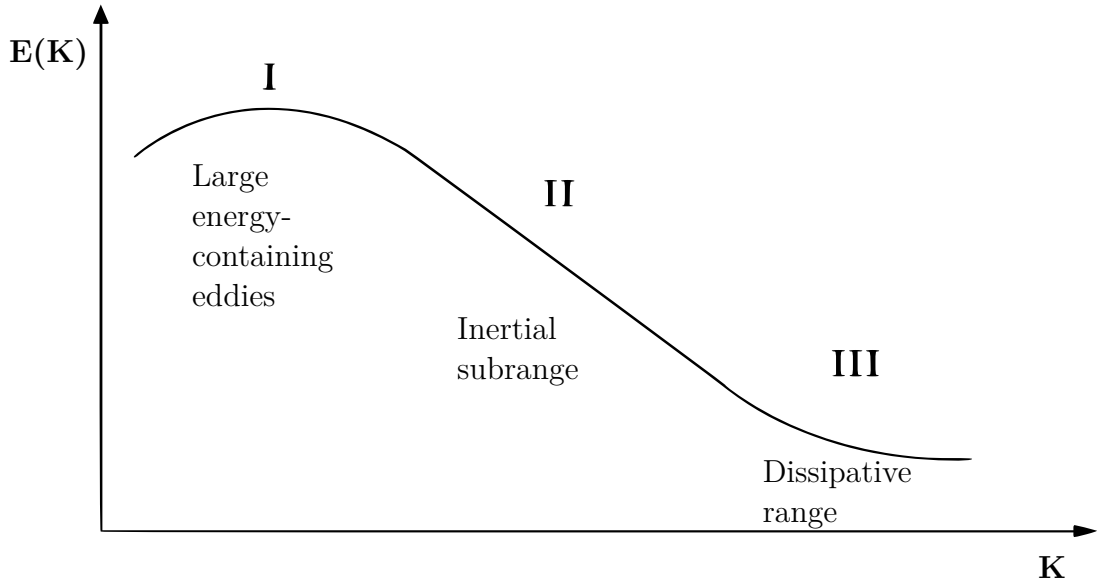

Figure 2.7: Spectrum of turbulent kinetic energy [17]

Reynolds- averaged Navier-Stoke equations
The most common approach for industrial applications is the Reynolds- decomposition of flow variables. They are divided into a mean value and a fluctuation Equation (2.13). The mean value is given by Equation (2.14) and indicates the assumption that the mean of the fluctuation is zero. The density weighted Favre- averaging results in simpler equations for incompressible flows Equation (2.15)- Equation (2.17) [12].

Reynolds- averaging [11]

$$u = \bar{u} + u' \tag{2.13}$$

$$\bar{u}(\mathrm{x}, t) = \frac{1}{t_\mathrm{g}} \int_{t=t_0}^{t_0+t_\mathrm{g}} u(\mathrm{x}, t)\mathrm{d}t \tag{2.14}$$

Favre- averaging [11]

$$u = \tilde{u} + u'' \tag{2.15}$$

$$\tilde{u} = \frac{\overline{\rho u}}{\bar{\rho}} \tag{2.16}$$

$$\widetilde{u}(\mathbf{x}, t) = \frac{1}{\bar{\rho}(\mathrm{x}, t)} \frac{1}{t_\mathrm{g}} \int_{t=t_0}^{t_0+t_\mathrm{g}} \rho(\mathrm{x}, t) u(\mathrm{x}, t)\mathrm{d}t \tag{2.17}$$

The substitution of the flow field variables with their mean values in the governing equations leads to the Reynolds-averaged Navier-Stokes equation (RANS)- equations Equation (2.18)- Equation (2.20). Therefore, a RANS simulation results in mean flow- and turbulence variables for the flow field. A suitable turbulence model must approximate

the effect of unresolved turbulence on the mean flow, called Reynolds- stresses [7]. The unclosed Reynolds-stress tensor is created as an effect of averaging the flow variables and is given by Equation (2.21). The flow field is considered to be a steady state. Unsteady Reynolds-averaged Navier-Stokes equation (URANS) have the ability to resolve the largest scales of a turbulent flow, but their time scales have to be much larger than the time scales of the turbulence model. [17].

RANS- equations [11]

$$\frac{\partial \bar{\rho}}{\partial t} + \frac{\partial}{\partial x_i}\left(\bar{\rho}\widetilde{u}_i\right) = 0, \tag{2.18}$$

$$\frac{\partial}{\partial t}\left(\bar{\rho}\widetilde{u}_i\right) + \frac{\partial}{\partial x_j}\left(\bar{\rho}\widetilde{u}_i\widetilde{u}_j + \widetilde{\bar{\rho}u_i''u_j''}\right) = \frac{\partial \bar{\tau}_{ij}}{\partial x_j} - \frac{\partial \bar{p}}{\partial x_i} + \overline{\rho f_i} \tag{2.19}$$

$$\begin{aligned}\frac{\partial}{\partial t}(\bar{\rho}\widetilde{E}) + \frac{\partial}{\partial x_j}\left[\widetilde{u}_j(\bar{\rho}\widetilde{E} + \bar{p})\right] = \frac{\partial}{\partial x_j}\Big[\widetilde{u}_i\left(\bar{\tau}_{ij} - \overline{\rho u_i''u_j''}\right) \\ + \overline{u_i''\tau_{ij}} - \bar{q}_j - \overline{\rho u_j''h''} - \tfrac{1}{2}\overline{\rho u_i''u_i''u_j''}\Big] + \overline{\rho u_i f_i}\end{aligned} \tag{2.20}$$

$$\tau_{ij}^{\mathrm{t}} = -\widetilde{\bar{\rho}u_i''u_j''} \tag{2.21}$$

RANS- turbulence models

Generally, RANS models are classified into eddy viscosity models and Reynolds stress models. They differ in their approach to solving the unknown Reynolds stresses. Eddy viscosity models use algebraic equations that correlate the unclosed terms with known averaged properties. Most models are based on the linear Boussinesq- hypothesis Equation (2.23). That assumes that the turbulent shear stress is related linearly to the mean strain rate Equation (2.24). The proportionality factor is the eddy viscosity [12]. The eddy viscosity models are differentiated in the number of transport equations to solve for turbulent length- and time scales that are needed to evaluate the eddy viscosity Equation (2.22). Reynolds-stress models (RSMs) solve one transport equation for each Reynolds stress. Therefore, they can eliminate some disadvantages from the eddy-viscosity models but need more computational resources [11]. Table 2.1 presents an overview of selected models.

$$\mu_{\mathrm{t}} \sim u_{\mathrm{t}} l_{\mathrm{t}} \tag{2.22}$$

$$\tau_{ij}^{\mathrm{t}} = -\widetilde{\bar{\rho}u_i''u_j''} \approx 2\mu_{\mathrm{t}}\widetilde{S}_{ij} - \delta_{ij}\frac{2}{3}\left(\mu_{\mathrm{t}}\frac{\partial \widetilde{u}_k}{\partial x_k} + \bar{\rho}k\right) \tag{2.23}$$

$$\widetilde{S}_{ij} \equiv \frac{1}{2}\left(\frac{\partial \widetilde{u}_i}{\partial x_j} + \frac{\partial \widetilde{u}_j}{\partial x_i}\right) \tag{2.24}$$

The dynamic viscosity coefficient μ in the viscous stress tensor Equation (2.19) can be replaced by the sum of the laminar and a turbulent component Equation (2.25) [12].

$$\mu = \mu_l + \mu_t \tag{2.25}$$

specific turbulent kinetic energy

$$k = \frac{1}{2}\frac{\overline{\rho u_i'' u_i''}}{\bar{\rho}} \tag{2.26}$$

Table 2.1: Overview Turbulence Models [11, 16, 18]

Eddy Viscosity Models	0-equation models	Cebeci- Smith model Baldwin-Lomax model Johnson-King model
	1- equation models	Prandtl's- one equation model Baldwin-Barth model Spalart- Allmaras model
	2-equation model	k-ϵ model k-ω model k-ω-SST model
Reynolds- stress- transport models		

In this work, the Spalart- Allmaras model and the k-ω-SST model are used for turbulence modeling.

Spalart- Allmaras model
Unlike other one-equation models, Spalart and Allmaras developed a model that directly solves a transport equation for turbulent viscosity. One advantage compared to algebraic zero-equation models and early one-equation modes is that it is local. The solution in one specific point is independent of the solution of other points. Therefore, it is compatible with grids of any structure. The Spalart- Allmaras model is numerically stable regarding near-wall resolution and stiffness. Two-equation models usually require finer grid resolutions near the wall. This leads to a higher computational effort than the second differential equation. For exceptional cases like aerodynamic simulations of airfoil flows, the Spalart-Allmaras model is an efficient and well-suited method [18].

k-ω-SST model
The k-ϵ- and k-ω-models are widely used two-equation models. The k-ϵ model focuses on turbulence kinetic energy, while the k-ω model emphasizes the turbulent kinetic energy dissipation rate. It has been shown by [19] that the behavior of the k-ω-model in the logarithmic region is superior to that of the k-ϵ-model in equilibrium adverse pressure gradient flows and incompressible flows. On the other hand, the k-ω model has an extreme sensitivity to the free stream values ω_f specified for ω outside the boundary layer. Menter [20] developed the Shear-Stress Transport (SST) turbulence model by using the robust and accurate formulation of the Wilcox k-ω-model in the near wall region and to take advantage of the freestream independence of the k-ϵ-model in the outer part of

the boundary layer. Therefore, the k-ϵ model is transformed into a k-ω formulation. An additional cross-diffusion term appears in the ω-equation. The Baseline Model (BSL) is created by adding the original k-ω-model and the transformed k-ϵ-model and weighing them by a blending function $F1$ and $(1 - F1)$, respectively. The function $F1$ is designed to be one in the near-wall region and zero in the free stream and wake regions. Therefore, the original model is activated near the surfaces and deactivated away from the surfaces. In the second step, the eddy viscosity definition will be modified to account for the transport of the principal turbulent shear stress. That is called the SST model [20].

2.3.4 Droplets

The droplet trajectories and impingement data are calculated with a multiphase simulation [21]. For the numerical modeling, multiphase flows are usually distinguished by their topology. Dispersed multiphase flows are characterized by particles or droplets dispersed in a continuous phase. In stratified flows, the phases are separated by distinct boundary surfaces. There are two main numerical approaches for dispersed multiphase flows. The first one is an Euler- Lagrangian method. The continuous phase is calculated by using the Eulerian method. The particles are tracked by using the Lagrangian method. In the second approach, both the droplets and the continuous phase are modeled by using the Eulerian method. The phases are weighted by their volume fraction α. For icing, the droplets are considered to be particles in a continuous flow using the Eulerian method for both phases. [21].

Particle Transport System
The mathematical model has been introduced by Bourgault et al. [22]. It is a two-fluid model consisting of the Euler or Navier-Stokes equations augmented by the particle continuity, Equation (2.27) and momentum Equation (2.28) equations. The two terms in the right-hand sight of the momentum equation are referred to as droplet drag and buoyancy forces. Spherical droplets at the MVD of the sample size distribution are assumed. The drag model for spherical droplets depends on the droplet Reynolds number. The equations are given by Equation (2.32) and Equation (2.29). The spherical droplet approximation is valid for droplet Reynolds numbers below 500. No collision or mixing between the droplets is accounted for, as these are insignificant in certification icing situations [23].

$$\frac{\partial \alpha}{\partial t} + \nabla \cdot (\alpha u_d) = 0 \tag{2.27}$$

$$\frac{\partial u_d}{\partial t} + u_d \cdot \nabla u_d = \frac{c_{d_d} Re_d}{24K} (u_a - u_d) + \left(1 - \frac{\rho_a}{\rho_w}\right) \frac{1}{Fr^2} g \tag{2.28}$$

Droplets Reynolds number [21]

$$\mathrm{Re}_d = \frac{\rho_a d u_a \left\| u_a - u_d \right\|}{\mu_a} \tag{2.29}$$

Inertial parameter
K is an inertial parameter of the droplets [21].

$$K = \frac{\rho_d d^2 u_a}{18 L_\infty \mu_a} \tag{2.30}$$

Froude number
The Froude numberdescribes the ratio of inertial force to gravity. [24]

$$Fr = \frac{\|u_a\|}{\sqrt{lg}} \tag{2.31}$$

Drag model[21]

$$\begin{aligned} C_D &= (24/\,\mathrm{Re}_d)\left(1 + 0.15\mathrm{Re}_d^{0.687}\right) \text{ for } \mathrm{Re}_d \leq 1300 \\ C_D &= 0.4 \quad \text{for } \mathrm{Re}_d > 1300 \end{aligned} \tag{2.32}$$

2.3.5 Icing

The icing model solves for the ice accretion, and runback water [21]. It is a conversion of the classical Messinger model [25] for thermal analysis of a heated surface in icing conditions into a system of Partial differential equations (PDEs). The first one is given by Equation (2.35) and refers to the conservation of mass. The second one is given by Equation (2.36) and refers to the conservation of energy. The icing model needs information about the frictional forces, the wall heat flux, and the caught water mass rate [26].

Linear velocity profil
The film thickness in icing simulations is usually very thin. Therefore, the velocity profile is simplified to a linear approach with zero velocity at the wall. The shear stress from the air is the main driving force for the water film. The linear velocity profile approach is given by Equation (2.33) [26].

$$u_f(x,y) = \frac{y}{\mu_w} \cdot \tau_{wall}(x,y) \tag{2.33}$$

Mean water film velocity
A mean velocity is obtained by averaging the velocity profile along the film thickness and given by Equation (2.34) [26].

$$\bar{u}_f(x,y) = \frac{1}{h_f}\int_0^{h_f} u_f(x,y)dy = \frac{h_f}{2\mu_w}\tau_{\text{wall}}\,(x,y) \tag{2.34}$$

Conservation Equations
In the mass conservation equation Equation (2.35), the first terms on the right-hand side correspond to the mass transfer by water droplet impingement. This is considered a source for the film. The second and third terms correspond to evaporation and ice accretion. They are considered a sink for the film. [26].

$$\rho_w\left[\frac{\partial h_f}{\partial t} + \nabla\cdot(\bar{u}_f h_f)\right] = u_\infty \cdot LWC \cdot \beta - \dot{m}_{\text{evap}} - \dot{m}_{ice} \tag{2.35}$$

The first three terms on the right-hand- side of the energy conservation equation correspond to the heat transfer caused by the supercooled water droplets impingement, the evaporation, and the ice accretion, respectively. The last two terms represent the radiative and convective heat transfer [26]. The heat and mass transfer phenomena used by the model is shown in Figure 2.8.

$$\begin{aligned}\rho_w \left[\frac{\partial h_f \cdot C_w \cdot \tilde{T}}{\partial t} + \nabla \cdot \left(u_f \cdot h_f \cdot C_w \cdot \tilde{T}\right)\right] = &\left[C_w \cdot \tilde{T}_{d,\infty} + \frac{\|u_d\|^2}{2}\right] \times u_\infty \cdot LWC \cdot \beta \\ &- 0.5 \cdot (L_{\text{evap}} + L_{\text{subl}}) \cdot \dot{m}_{\text{evap}} \\ &+ \left(L_{\text{fusion}} - C_{\text{ice}} \cdot \tilde{T}\right) \cdot \dot{m}_{ice} \\ &+ \epsilon \cdot \sigma \cdot \left(T_\infty^4 - T^4\right) + \dot{Q}_h\end{aligned} \tag{2.36}$$

Droplet collection efficiency
The droplet trajectory solver determines the droplet collection efficiency [26].

$$\beta = -\frac{\alpha u_d \cdot \vec{n}}{(LWC_\infty)\, u_\infty} \tag{2.37}$$

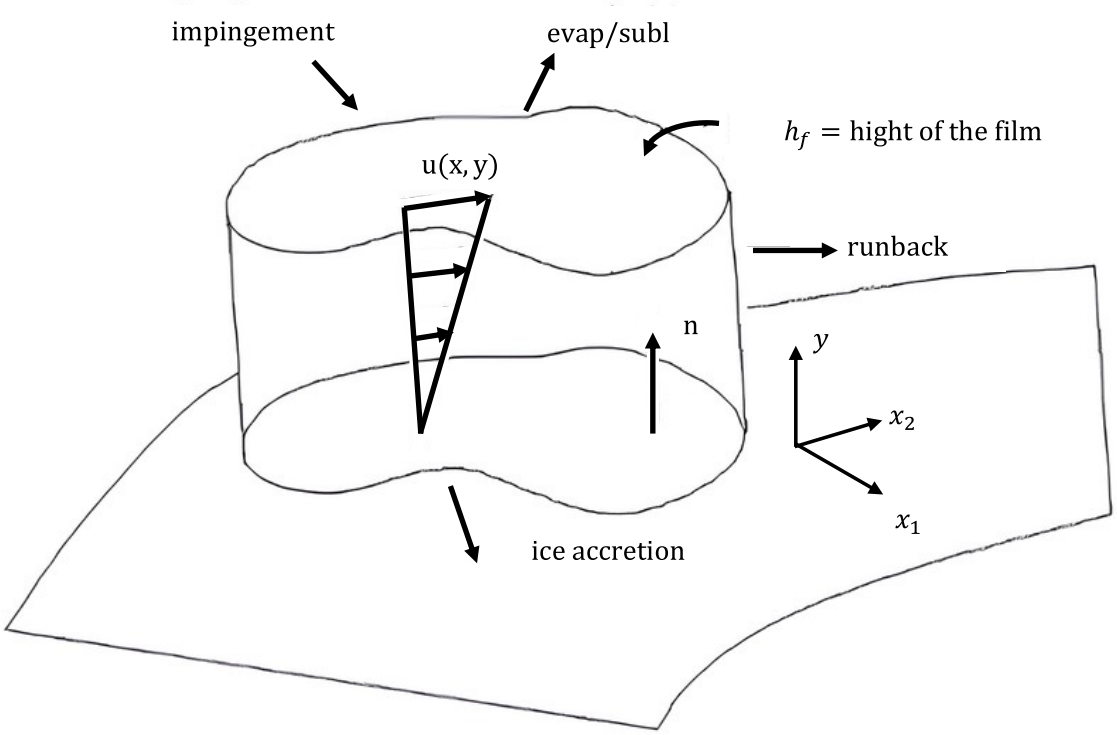

Figure 2.8: Heat and mass balance in a thin film [27].

2.4 Grid Convergence Study

Various approximations are made during model development and solution. The errors made in the process add up to a total error. That is divided into a discretization error and an iteration error. Residuals can estimate the iteration error. The discretization error is more difficult to estimate. The Richardson extrapolation can be used to estimate the exact numerical value from the converged solutions of three grids of different fineness with a constant discretization parameter. It is assumed that the discretization error is significantly larger than the iteration error. Furthermore, it is required that the solution converges monotonically towards the numerically exact value as the mesh becomes finer. The assessment helps to weigh up the additional effort required against the additional quality of the solution that can be achieved by a finer grid [7].

The definition of the discretization parameter h is not always clear [7]. f_1 - f_3 are the converged solutions of the different grids. f_1 refers to the finest grid, f_2 to the medium grid and f_3 to the coarse grid. $f_{h=0}$ is the estimation of the exact numerical solution and is given by Equation (2.40) p describes the order of convergence and is given by Equation (2.39).

$$r = h_2/h_1 \tag{2.38}$$

$$p = \ln\left(\frac{f_3 - f_2}{f_2 - f_1}\right) / \ln(r) \tag{2.39}$$

$$f_{h=0} \cong f_1 + \frac{f_1 - f_2}{\tau^p - 1} \tag{2.40}$$

Roache et al. [28] introduced the concept of a Grid convergence index (GCI) to provide an error band on the grid convergence of the solution of Equation (2.42). It indicates how much the solution would change with a further refinement of the grid. A small value of GCI indicates that the computation is within the asymptotic range. ϵ in Equation (2.41) describes the relative error [29].

$$\varepsilon = \frac{f_2 - f_1}{f_1} \tag{2.41}$$

$$\mathrm{GCI}_{\mathrm{fine}} = \frac{F_s|\varepsilon|}{(r^p - 1)} \tag{2.42}$$

$$\mathrm{GCI}_{\mathrm{coarse}} = \frac{F_s|\epsilon|r^p}{(r^p - 1)} \tag{2.43}$$

3 Methods

The work is structured into three main parts.

1. Reverse engineering of the Skywalker X8
The first main part is the Computer aided design (CAD) reverse-engineering of the Skywalker X8-UAV. This is based on an online available 3D-scan [30] and a cut wing for reference cross-section. These are scanned on a conventional printer and used to validate the scaling of the 3D-scan. Additionally they are used as a reference for the cross-section profils in the model, to get a CAD- model, which is suitable for the CFD- analysis.

2. Grid convergence study on S5010 reference airfoil
The second part consists of a grid convergence study based on a reference airfoil with available wind tunnel data for lift- and drag coefficients. XFLR5 is used for further validation.

3. CFD- performance loss analysis of the X8-664 airfoil due to icing
The third part consists of the numerical investigation of the performance degradation due to in-flight icing on a representative cross-section of the Skywalker X8 wing, which has been tested in an IWT before. The numerical results are compared to the IWT- ice geometry using a photogrammetry method to digitize the ice shapes. Three different temperatures were tested in the IWT for glaze ice (−2 °C), mixed ice (−4 °C) and rime ice (−10 °C). These are investigated at an air speed of 25 $\mathrm{m\,s^{-1}}$. The exact reference pressure in the IWT is unknown but approximately ambient pressure. More details for the air properties are given in Table 3.1. A reference flow with the reference airfoil is investigated at 20 °C and 16.2 $\mathrm{m\,s^{-1}}$. XFLR5 is used for further validation.

Table 3.1: Icing conditions air

Regime	Case	Temperature	Velocity	Pressure	Reynolds number
-	Reference flow	20 °C	16.2 $\mathrm{m\,s^{-1}}$	101325 Pa	300129
Glaze ice	IWT	−2 °C	25 $\mathrm{m\,s^{-1}}$	101325 Pa	561080
Mixed ice	IWT	−4 °C	25 $\mathrm{m\,s^{-1}}$	101325 Pa	538860
Rime ice	IWT	−10 °C	25 $\mathrm{m\,s^{-1}}$	101325 Pa	531770

The LWC describes the density of water droplets in the air. In the IWT tests a LWC of 0.52 $\mathrm{g\,m^{-3}}$ is used. A custom droplet distribution is applied. The distribution is described by the droplet size of its MVD and their respective weight in % of LWC. The icing time in the IWT is 1200 s. The droplet distribution is given in Table 3.3.

Table 3.2: Icing conditions droplets

Property	**Value**
LWC	$0.52\ \mathrm{g\,m^{-3}}$
Water density	$1000\ \mathrm{kg\,m^{-3}}$
Droplet distribution	Custom distribution
Icing time	1200 s

Table 3.3: Droplet distribution

Droplet diameter in µm	**Weight in % of LWC**
90.2	5
61.3	10
39	20
26.9	30
18.7	20
12.6	10
7.5	5

3.1 FENSAP-ICE

Ansys FENSAP-ICE is a state-of-the-art CFD software developed for in-flight icing. It consists of six main modules. Three of those are used to evaluate the aerodynamic performance of the clean airfoil, the iced airfoil, and the ice accretion [21].

FENSAP
FENSAP is a 3D finite element Navier-Stokes solver for the flow field. It solves the system of PDE described in Section 2.3.1. A RANS- solution is performed for turbulent flows, which is described in Section 2.3.3. The solutions for the velocity, the wall heat fluxes, and the wall shear stresses are essential for the following droplet impingement and ice accretion [21].

DROP3D
DROP3D is a 3D finite element droplet impingement solver. It solves the particle flow as a continuum, using the Eulerian formulation described in Section 2.3.4. The ice accretion

solver uses the results of the droplet impingement solution [21].

ICE3D
ICE3D is a 3D finite-volume ice accretion and runback water solver. The heat and mass transfer phenomena that are accounted for are based on the Messinger model and described in Section 2.3.5 [21]

Process from clean performance to iced performance
The analysis of the aerodynamic performance loss is performed in three main steps. At first, the performance data of the clean, smooth, and, therefore, undisturbed airfoil are calculated. The second step is the calculation of the ice accretion on the airfoil. The iced geometry is used to evaluate the performance loss in atmospheric icing conditions. These three steps are shown in Figure 3.1.

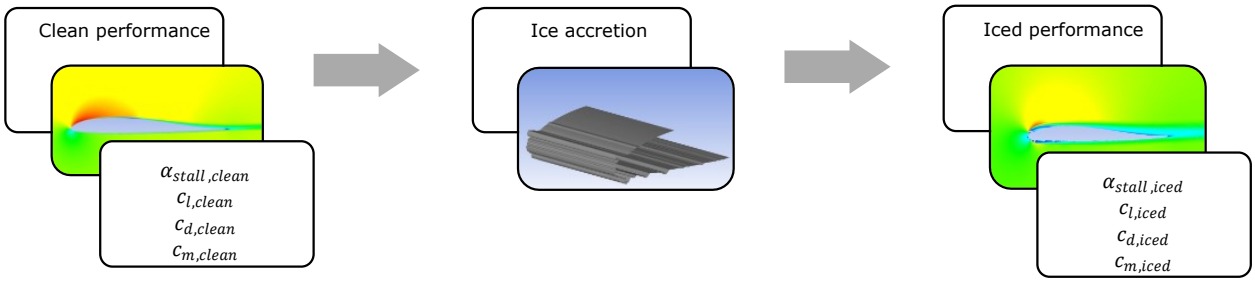

Figure 3.1: FENSAP-ICE from clean performance to iced performance

Multishot ice accretion simulation

FENSAP, DROP3D, and ICE3D can be used in standalone mode or in a sequence with multiple time steps, which is called a multishot simulation. In a multishot simulation, the ice accretion time is split into several time steps. Each time step consists of the consecutive solution of the flow field, the droplet impingement, the ice accretion, and the mesh of the iced geometry. Figure 3.2 shows how the modules interact with each other.

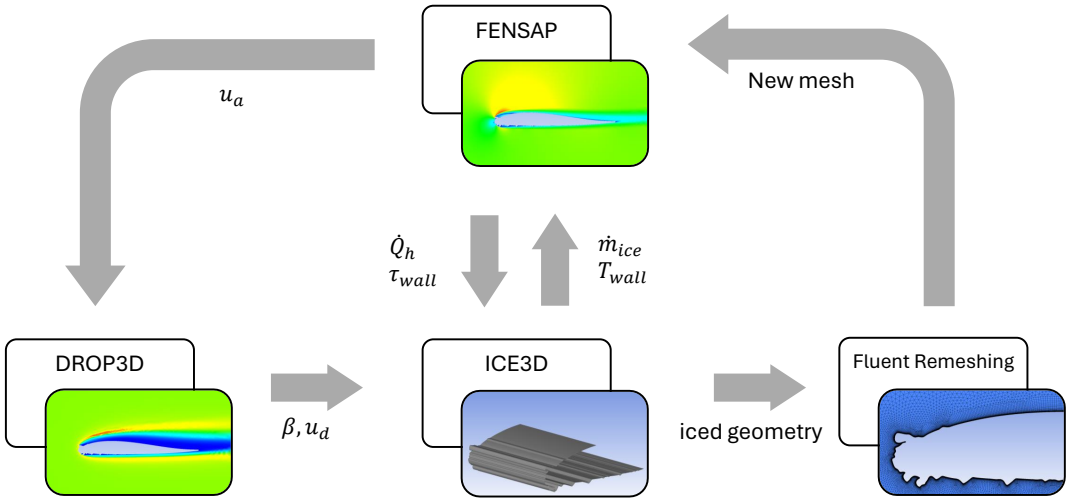

Figure 3.2: FENSAP-ICE Sequence Simulation [27]

3.2 Geometry Skywalker X8

One main objective of this work is a reverse-engineered 3D CAD model of the Skywalker X8 to obtain a suitable CAD model for CFD analysis.
The reverse engineering of the Skywalker X8 is mainly based on the model of a publicly available 3D scan model that already exists, shown in Figure 3.3 and a cut wing, which is shown in Figure 3.4 (a). The cross-sections of the cut wing are scanned on a conventional printer and imported into Catia V5, which is used as the CAD program, Figure 3.4 (b). Since the dimensions of the printer scans are known precisely, they are used to validate the 3D scan model. The goal is to match the 3D scan, the printer scan, and the reverse-engineered surface. An example of that procedure is shown in Figure 3.4 (d). The orange and violet splines represent the suction and pressure side of the airfoil. They match the intersected scan at $Y = 210$ mm in green and are used to design the fuselage and the wing. The pink airfoil represents the intersection with the scan at $Y = 210$ mm and matches the belonging printer scan. The wing is designed based on three cross-sections in the wing and two for the winglets. Additionally, one guide curve at the LE and two at the TE are used. The airfoils for the wing are positioned in a spanwise direction at $Y = 197$ mm, $Y = 500$ mm and $Y = 1000$ mm. The middle cross-section of the section investigated in the IWT is located at $Y = 664$ mm. Therefore, the re-designed representative IWT airfoil is named X8-664. The wing root airfoil at $Y = 197$ mm is designed with the outer cross-section of the fuselage, as this matched the printer scans better. The airfoils are designed with two 7^{th}- order B-splines to achieve a highly continuous and well-controllable profile. One is for the suction and pressure side, respectively, Figure 3.4(c). The LE is connected with a tangential surface. This is shown in Figure 3.5 (a). The fuselage is designed with three airfoil-shaped cross-sections and six guide curves, Figure 3.5 (b). An example of the design of the guide curves is shown in Figure 3.4 (e). The wing and the fuselage are modeled separately, but all surfaces are closed and connected and, therefore, directly usable for CFD analysis. The geometry is partially simplified at structural component boundaries, flaps, and covers to reduce the meshing- and thus calculation effort.

Figure 3.3: Scan Skywalker X8 [30]

(a)

(b)

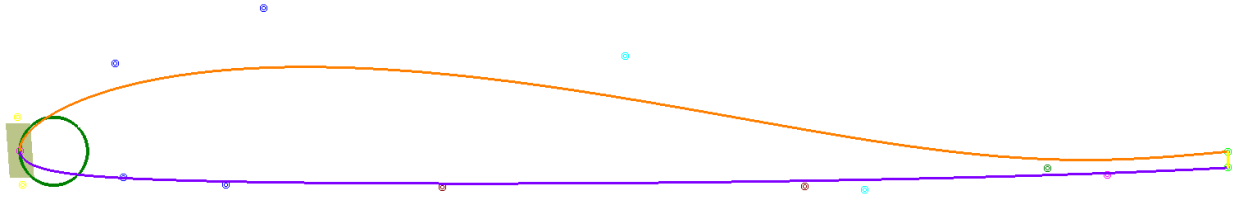

(c)

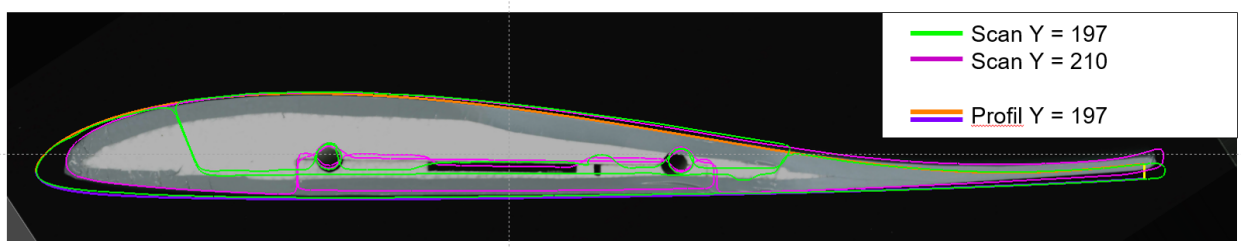

(d)

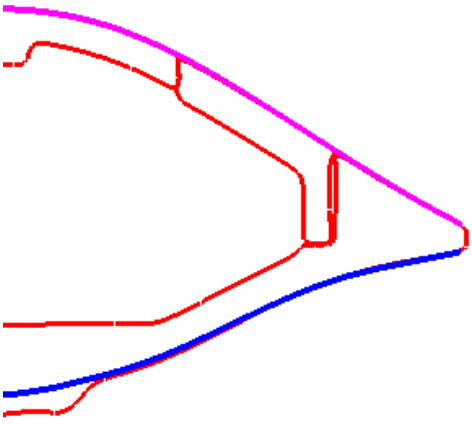

(e)

Figure 3.4: (a) Cutted Skywalker X8 wing, (b) Cross-section printer scan, (c) Airfoil spline design, (d) Matching process, (e) Fuselage cross-section spline design in YZ-Plane

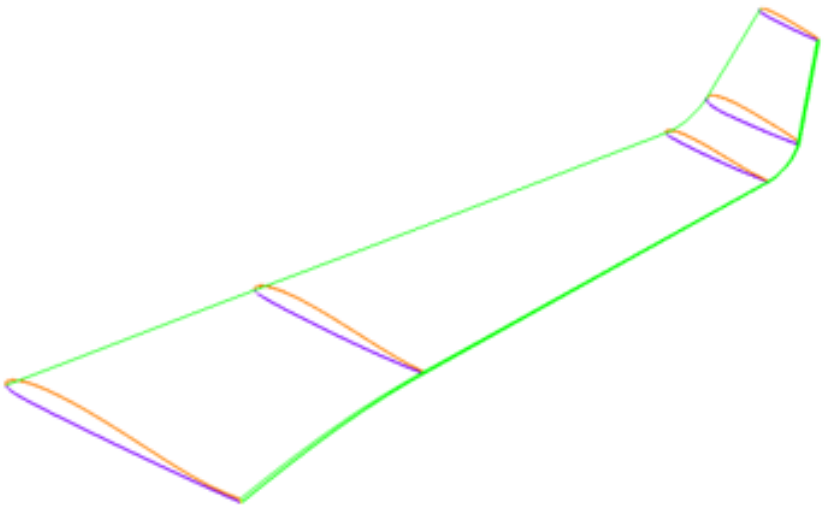

(a)

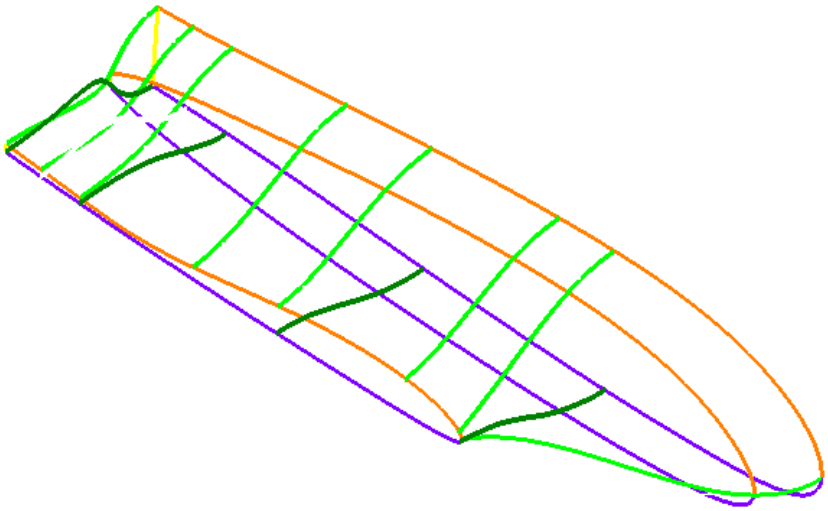

(b)

Figure 3.5: (a) Strak wing, (b) Strak fuselage

3.3 Methods for Validation

Since the exact airfoil of the Skywalker X8- UAV is unknown, and no aerodynamic test data are available, it is difficult to assess the quality of the CFD- results regarding lift- drag- and momentum coefficient. Therefore, the needed spatial discretization and the clean airfoil performance model setup are investigated with a comparable reference airfoil, for which wind tunnel data are available. The S5010 low-speed airfoil for flying wings by Selig et al. [31] is found. Additionally, XFLR5 is used as a second numerical tool to compare the clean airfoil performance for the S5010 and X8-664 airfoils. For transition the e^n method using $n_{crit} = 9$.

Reference Airfoil

The 5010 airfoil by Selig et al. has a sharp TE. Therefore, it is adapted with a 2.1 mm blunt trailing edge. Wind-tunnel data for lift- and drag- coefficient are given by Selig et al. [31] for $Re = 60000$ to $Re = 300000$. Since the Reynolds- number in the investigated in-flight icing cases of the Skywalker X8 airfoil is approximately $Re \approx 550,000$, the BL will develop differently. Therefore, the grid setup with the reference airfoil is considered preliminary and must be reviewed with the X8-664 airfoil, mainly focusing on the y^+- value.

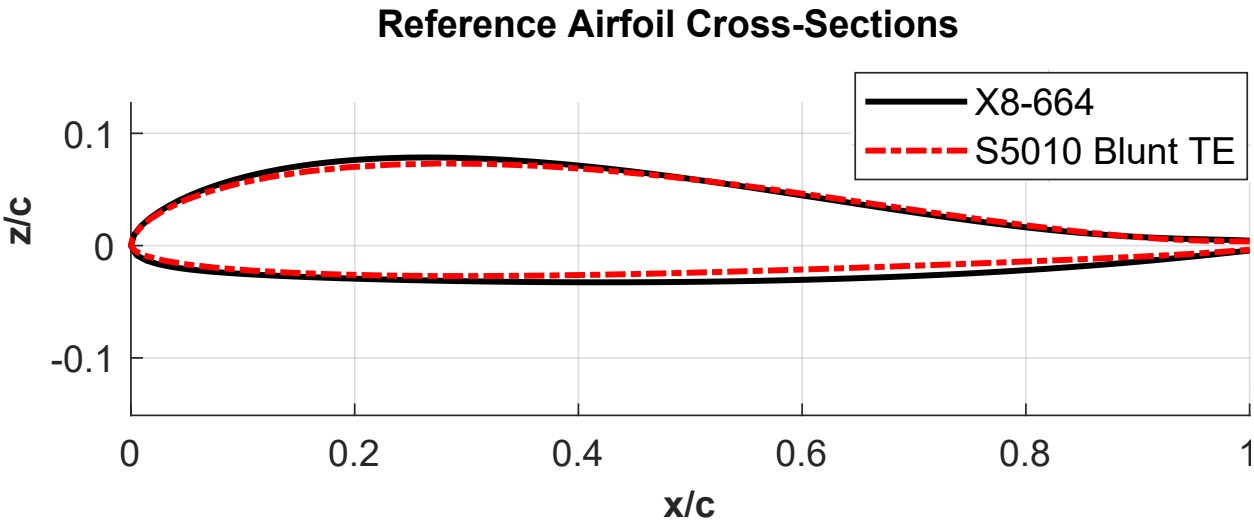

Figure 3.6: Reference Profile [31]

Photogrammetry

Digital 3D models are created from the ice shapes measured in the IWT using structure-from-Motion (SfM) photogrammetry. Further details on SfM can be found in [32]. These are cut at various positions in the profile section, Figure 3.7 and projected onto a plane. An envelope is placed around the resulting projections, Figure 3.8. This is known as MCCS and, according to Lee et al. [33], the digital equivalent to the traditional hand-tracing method, which usually reflects the maximum outer boundary of the ice shape. The preparation of the digital model and the MCCS are not part of this work and are provided internally.

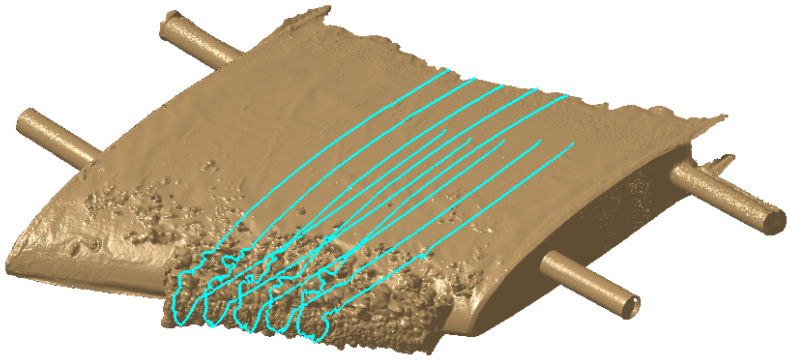

Figure 3.7: MCCS cuts

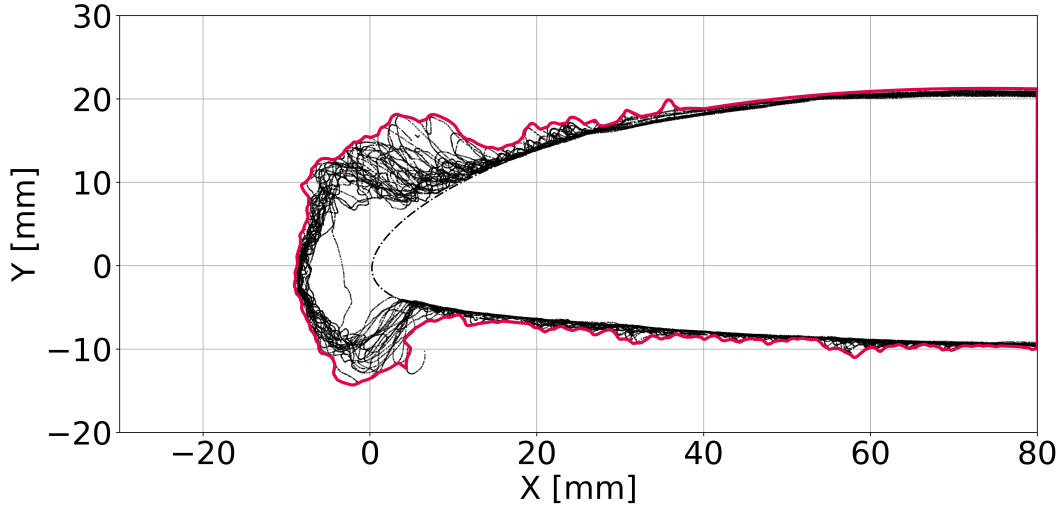

Figure 3.8: MCCS envelope

3.4 Fluid Domain and Boundary Conditions

Fluid Domain
A hybrid O-grid is used for the fluid domain of the 2D icing simulation of the airfoils. The unstructured triangular mesh in the far field merges into a structured rectangular mesh to resolve to the boundary layer with $y^+ < 1$. A schematic example of the hybrid O-grid structure is shown in Figure 3.9 (a). Fluent Remesh requires a thickness of one layer. Therefore, a 2.5D grid is created by extruding the 2D- grid by 0.1 m. The diameter of the fluid domain is 27.9 m. The thickness of the fluid domain is schematically shown in Figure 3.9 (b).

Boundary Conditions
The Boundary condition (BC) are a pressure inlet at the ring surface, which is represented in red in Figure 3.9 (b), a symmetry- BC at the circular surface in blue in Figure 3.9 (b), and no-slip walls at the airfoil in gray in Figure 3.9 (b-d). A second symmetry- BC is located parallel to the visible one. The airfoil walls are split into a surface around the LE where icing is enabled, Figure 3.9 (c), and a surface around the TE where icing is disabled, Figure 3.9 (d). The pressure inlet contains a constant velocity, pressure, and temperature. The velocity components are calculated with the defined angle of attack.

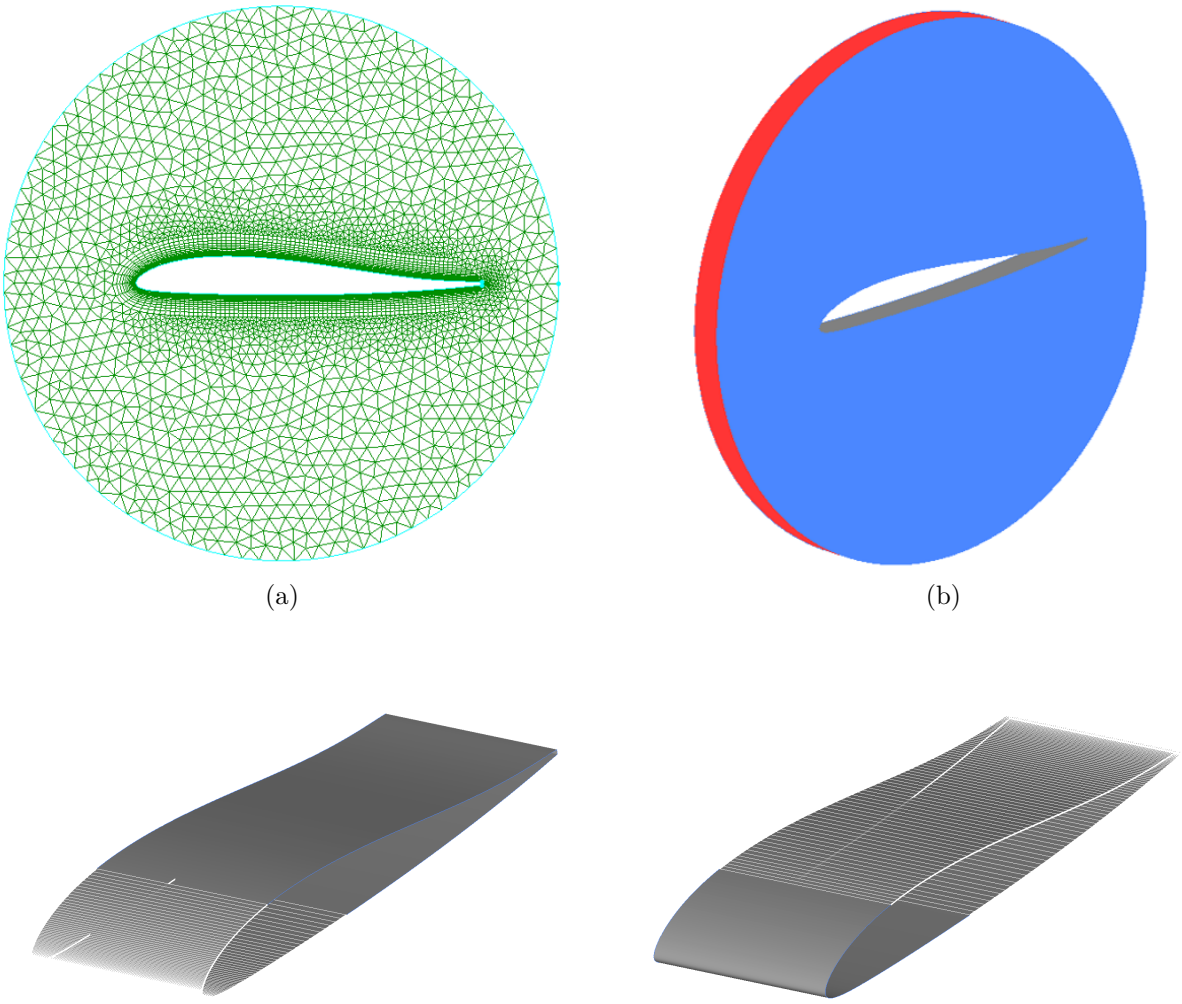

(a) (b)

(c) (d)

Figure 3.9: (a) Schematic hybrid O-grid, (b) Schematic 2.5D fluid domain, (c) Airfoil wall with enabled icing, (d) Airfoil wall with disabled icing

3.5 Clean Airfoil Performance Model

A baseline is first calculated on the clean airfoil to analyze the aerodynamic performance losses on the iced airfoil. Since only a flow field solution is needed, FENSAP is used in standalone mode.

3.5.1 Numerical Model Setup

For the clean airfoil performance model, FENSAP is used in standalone mode. The clean airfoil performance model is set up with the S5010 reference airfoil at a Reynolds number of $Re = 300,000$. This corresponds to a velocity of 16.2 $\mathrm{m\,s^{-1}}$ at a temperature of 20 °C. Additionally, a grid convergence study was performed using this setup, wich is explained in more detail in Section 3.5.2. Although the Reynolds numbers for X8-664 analysis of the rime ice, mixed ice, and glaze ice cases differ slightly due to the temperature difference but constant velocity, no significant difference in the numerical aerodynamic performance can be observed. Therefore, the mixed ice case is used as a reference for the clean performance of the X8-664 profile. The corresponding Reynolds number is $Re = 539,000$ at 25 $\mathrm{m\,s^{-1}}$ and −4 °C. To model the turbulence, the $k\omega$-SST model is used in combination with intermittency for transition. Since the clean case should account for the undisturbed performance no surface roughness is applied. The wall temperature is set to adiabatic stagnation temperature +10 K for conventional reasons. The temperature is used for the correct calculation of the heat flux [21]. The Courant–Friedrichs–Lewy (CFL) number of 200 is used with a maximum of 1500 iterations. If convergence is good, a higher CFL number may be used to accelerate the simulation. The extrusion of the grid by 0.1 m results in a reference area of 0.0279 $\mathrm{m^2}$ with a chord length of 0.279 $\mathrm{m^2}$. To determine the pitching moment, the hinge point is located at the $c/4$ point at half of the extrusion in z. Further details on the setup are given in Table 3.4. The structure of the table is based on the procedure in FENSAP.

Table 3.4: Numerical FENSAP setup for the clean airfoil performance model

Model	
Physical model	Air
Momentum equation	Navier- Stokes
Energy equation	Full PDE
Turbulence model	kω-SST
Surface roughness	No roughness
Transition	Intermittency
Conditions	
Characteristic length	0.279 m
Air velocity	Reference airfoil: 16.2 $\mathrm{m\,s^{-1}}$
	IWT: 25 $\mathrm{m\,s^{-1}}$
Air static pressure	101325 Pa
Air static temperature	Reference: 293.15 K
	Mixed ice: 269.15 K
Initial solution	Velocity angles
Angle of attack	4° or Sweep
Boundaries	
Inlet	Reference conditions
Airfoil surface	Wall
	No- slip condition
	Temperature: Adiabatic stagnation temperature +10 K
Solver	
CFL number	200
Max. number of time steps	1500
Variable relaxation	300 time steps
Cross- wind dissipation	$1 \cdot 10^{-7}$
Forces	Drag direction based on inlet boundary condition
Reference area	$c \cdot b = 0.0279$ $\mathrm{m^2}$
Moment reference point-X	$c/4 = 0.06975$ m
Moment reference point-Z	$b/2 = 0.05$ m

3.5.2 Grid Convergence Study

Since the exact airfoil of the Skywalker-X8 is unknown, the grid dependence is analyzed with the comparable reference airfoil S5010. The three main aerodynamic properties, lift- drag and momentum coefficient, are investigated with three different grids. Pointwise V18.6R4 is used for the grid generation. A T-Rex mesh is used for the clean airfoil performance to generate anisotropic layers from the boundaries of unstructured domains [34].

The discretization parameter h is defined as the chord length c divided by the numbers of element n

$$h = c/n \tag{3.1}$$

Grid parameters that are required for a suitable mesh are kept constant and shown in Table 3.5. The far-field diameter is $100 \cdot c$ to minimize the influence of the far-field BC. An example of the grid of the whole fluid domain is shown in Figure 3.10 (a). Delta s describes the height of the first layer next to the airfoil wall BC. It is set to $5 \cdot 10^{-6}$ to achieve a $y^+ < 1$ for a sufficient boundary layer resolution. The max. layers parameter describes a target value of the structured layers. By using a high value, an automatic transition from the structured to the unstructured grid will be performed [34]. An example of the T-Rex mesh with the automatic transition is shown in Figure 3.10 (b). One full layer helps to control the mesh at the TE, Figure 3.10 (d). The values for decay and growth rate are found to be suitable.

Table 3.5: Grid convergence constant parameters

Constant Grid Parameter	**Value**
Chord length	0.279 m
Far-field diameter	$100 \cdot c = 27.9$ m
Delta s	$5 \cdot 10^{-6}$ m
Growth rate T-Rex	1.15
Max. layers	500
Full layers	1
Decay	0.95
Growth rate BC	1.15

The varied grid parameters are shown in Table 3.6. The refinement factor r is set to $\sqrt{2}$. The fine and coarse mesh are presented in Figure 3.11. All grids are refined to the LE- point and the TE. Examples are shown in Figure 3.10 (c) and (d).

Table 3.6: Grid convergence varied parameters

Constant Grid Parameter	**Fine**	**Medium**	**Coarse**
Points far-field	142	100	71
Points airfoil	227	160	114
Grid spacing LE in m	$7.07 \cdot 10^{-5}$	$1.0 \cdot 10^{-4}$	$1.4 \cdot 10^{-4}$
Grid spacing TE in m	$2.12 \cdot 10^{-4}$	$3.0 \cdot 10^{-4}$	$4.2 \cdot 10^{-4}$
Elements	115922	94424	77449

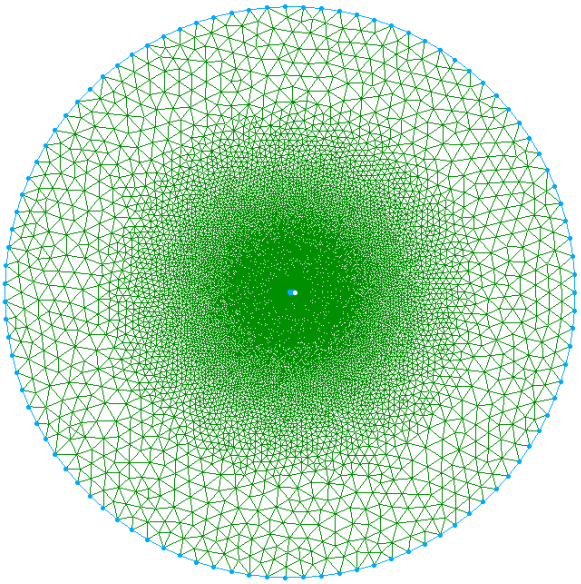

(a)

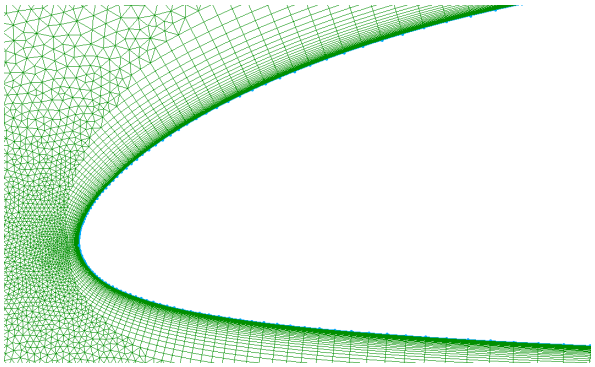

(b)

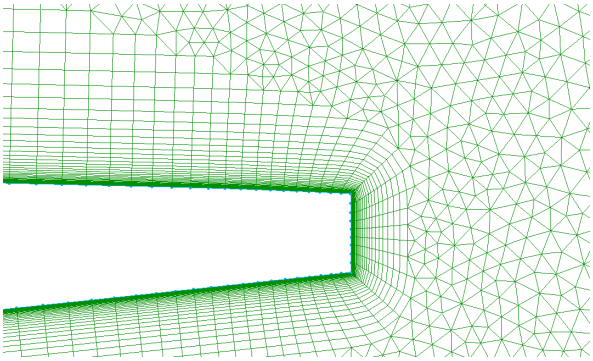

(c)

Figure 3.10: (a) Grid far-field, (b) Grid airfoil (c) Grid LE, (d) Grid TE

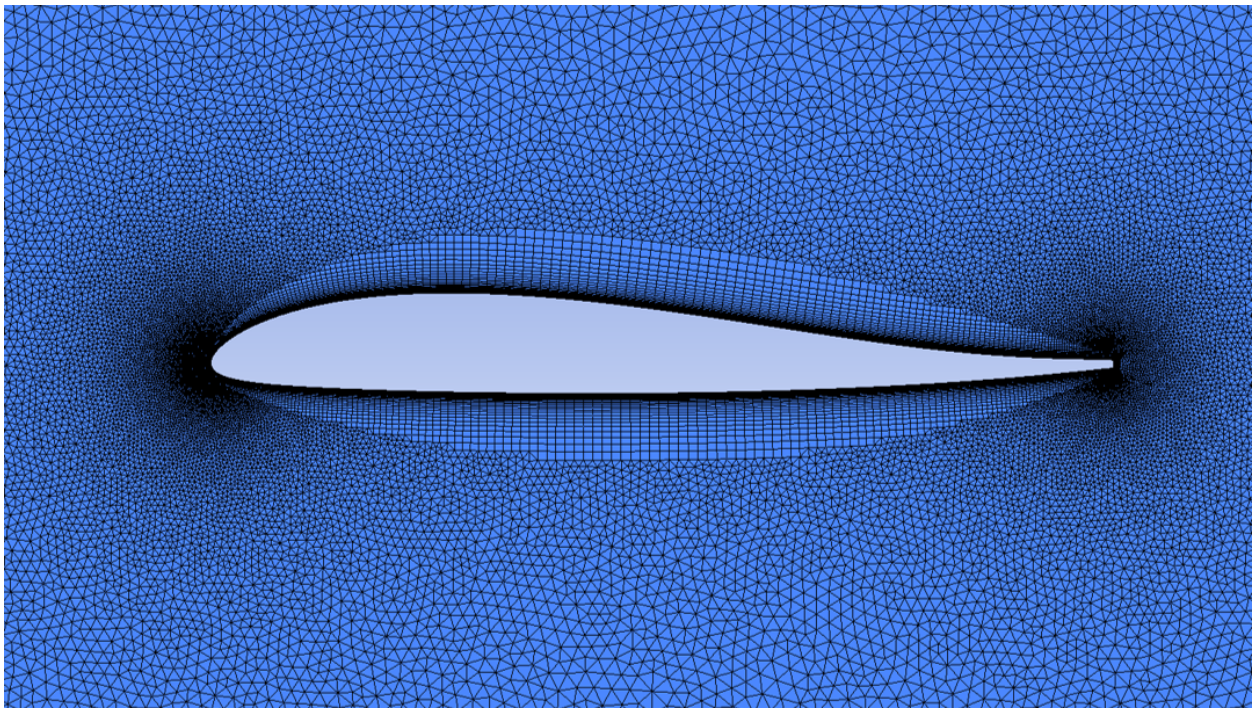

(a)

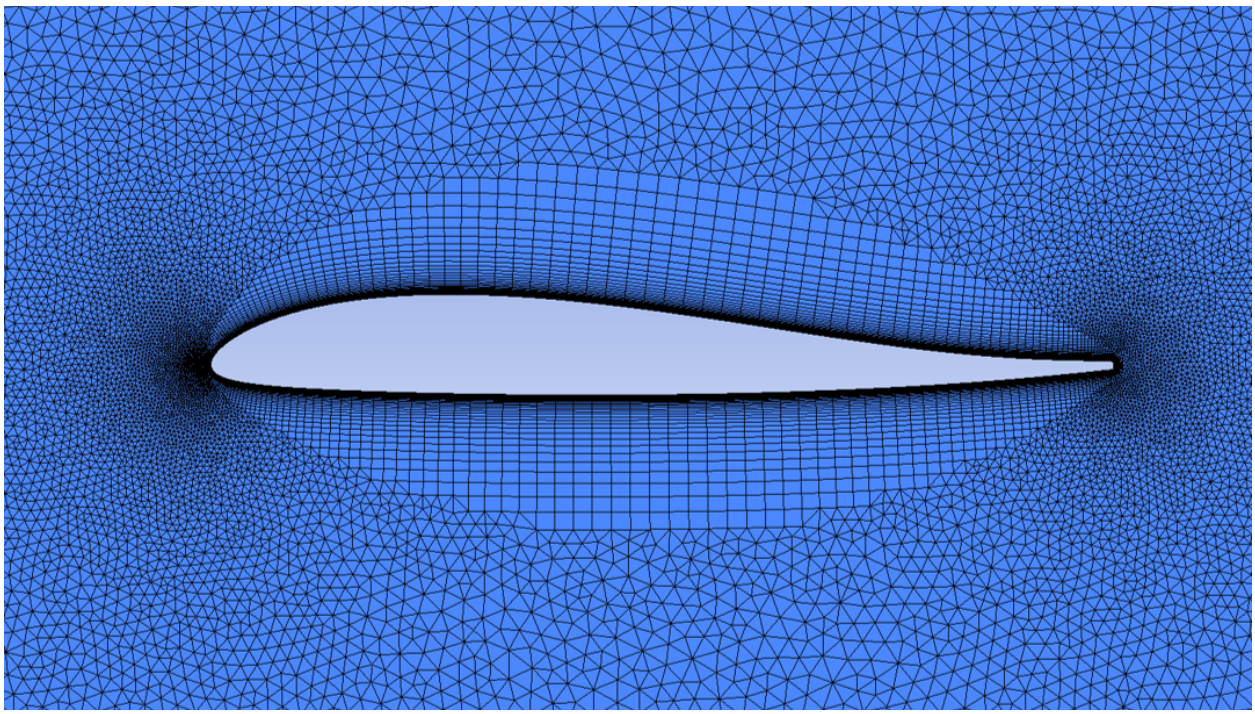

(b)

Figure 3.11: (a) Grid fine, (b) Grid coarse

3.6 Ice Accretion Model

FENSAP-ICE is used in sequence mode for the ice accretion simulation with FENSAP, DROP3D, ICE3D, and Fluent Meshing. The total icing time is set to 1200 s at an Angle of attack (AoA) of $\alpha = 4°$. according to the IWT test. The number of time steps for the glaze ice and rime ice cases is set to 15 and 49 time steps based on internal results. An additional time step study is carried out for the mixed ice case. Setting shorter time steps at the beginning of the calculation is recommended if the ice accretion simulation is based on a sandgrain-roughness flow solution to calculate more realistic ice shapes [21]. However, a compromise must be made with the computational costs. Therefore, the first time step is always set to 10 s.

Table 3.7: Time steps ice accretion

Case	**Time steps**	textbfDensity model
Glaze ice	15	Impact density
Mixed ice	15,30,49	Constant density/ Impact density (beta-function)
Rime ice	49	Constant density

3.6.1 Numerical Model Setup

FENSAP

A fully turbulent flow is assumed for the ice accretion simulation. To reduce the computational effort, the Spalart-Allmaras model is used for turbulence modeling. A sandgrain roughness of 0.4 mm is required as a basis for ice formation, which is why a sandgrain roughness of 0.4 mm is used. Further details are shown in Table 3.8. The settings that are not mentioned in this table can be taken from the numerical setup of the clean airfoil in Table 3.4.

Table 3.8: Numerical setup ice accretion model FENSAP

Model	
Turbulence model	Spalart-Allmaras
Surface roughness	Specified sandgrain roughness 0.4 mm
Transition	No transition

DROP3D

The reference conditions for the numerical model of DROP3D are taken over from FENSAP. Droplets are used for both the physical and the particle model. The water default model is used as the drag model for the droplets. The conditions are adopted based on the IWT test with a LWC value of 0.52 $\mathrm{g\,m^{-3}}$ and a droplet distribution, which is given in table Table 3.2. The density of the water droplets is set to 1000 $\mathrm{kg\,m^{-3}}$. Further details can be found in Table 3.9.

Table 3.9: Numerical setup ice accretion model DROP3D

Model	
Physical model	Droplets
Particle type	Droplets
Droplet drag model	Water-default
Conditions	
Reference conditions	Data takeover from FENSAP
LWC	0.52 $\mathrm{g\,m^{-3}}$
Water density	1000 $\mathrm{kg/m^3}$
Droplet distribution	Custom distribution see Table 3.3
Droplet initial solution	Velocity angles
Angle of attack	4°
Boundaries	
Inlet	Reference conditions
Solver	
CFL number	20
Maximum timesteps	200
Cross-wind dissipation	$1 \cdot 10^{-5}$

ICE3D

The glaze-advanced model with the classical heat flux type is used as the numerical setup for the ice accretion model. The beading model is activated since the ice accretion calculation is set up with sandgrain roughness. ICED3D will calculate the new roughness based on the local conditions and transfer it automatically to the flow solver for the correct calculation of the shear stresses and the heat fluxes. The reference conditions are taken over from FENSAP and DROP3D. The humidity is set to 95 % according to the IWT test. For the rime ice case, the constant density model is used with a density of 917 kg/m^3. The glaze ice case is calculated with the impact density model, which is a beta-function in FENSAP-ICE 2023 R2. To reduce the calculation costs, icing is only enabled at the LE- area. Thus, the airfoil wall- BC is split at 20 % at the suction surface and at 40 at the pressure surface. It is split unequally because more runback water is expected at the pressure surface at an AoA of $\alpha = 4°$. In the context of a multishot calculation, the total time of ice accretion is defined as the icing time per time step. The grid displacement generation after the completed timestep is activated and set to Fluent Meshing. The standard settings are given in Table 3.11

Table 3.10: Numerical setup ice accretion model ICE3D

Model	
Ice-Water model	Glaze-Advanced
Heat flux type	Classical
Beading	Activated
Conditions	
Reference conditions	Data takeover from FENSAP and DROP3D
Relative humidity	95%
Ice density type	Rime ice 263.15 K: Constant 917 $\mathrm{kg\,m^{-3}}$ Mixed ice 269.15 K: Constant 917 $\mathrm{kg\,m^{-3}}$/ Impact ice density Glaze ice 271.15 K: Impact ice density
Boundaries	
Airfoil wall LE	Icing enabled
Airfoil wall TE	Icing disabled
Solver	
Total time of ice accretion	Icing time per shot is default value for multishot iteration
Out	
Generate grid displacement	Yes
Grid displacement mode	Remeshing-Fluent Meshing

3.7 Iced Airfoil Performance Model

The iced performance model has the same structure as the clean airfoil. It is only extended by a surface roughness. The method is used via the sand-grain roughness file, which is taken from the previous ice accretion simulation. If the iced grid is to be refined for the performance calculation, the roughness must be interpolated from the old grid to the new one.

3.7.1 Grid Convergence Study for Iced Performance Model

For the iced performance model, a grid convergence study is performed similar to the clean airfoil study. Again, the three main aerodynamic variables, lift-drag and pitch moment coefficient, are considered on three different grids. The refinement factor is 2. This study uses Fluent Meshing based on the last iced grid. The corresponding parameters are given in Table 3.11. As described above, the roughness must be interpolated to the new grids.

Table 3.11: Settings grid convergence study X8-664 Fluent Meshing for iced performance

Parameter	**Standard**	**Medium**	**Fine**
globmin	$1 \cdot 10^{-5}$	$5 \cdot 10^{-6}$	$2.5 \cdot 10^{-6}$
proxmin	$1 \cdot 10^{-4}$	$5 \cdot 10^{-5}$	$2.5 \cdot 10^{-5}$
curvmin	$3 \cdot 10^{-4}$	$1.5 \cdot 10^{-4}$	$7.5 \cdot 10^{-5}$
curvleading	$7 \cdot 10^{-4}$	$3.5 \cdot 10^{-4}$	$1.75 \cdot 10^{-4}$
curvmax	$1 \cdot 10^{-3}$	$5 \cdot 10^{-4}$	$2.5 \cdot 10^{-4}$
globmax	0.3	0.3	0.3
nprisms	45	45	45
firstCellH	$2 \cdot 10^{-6}$	$2 \cdot 10^{-6}$	$2 \cdot 10^{-6}$
mpx	0.282	0.282	0.282
mpy	0	0	0
mpz	0.05	0.05	0.05
z-span	0.1	0.1	0.1
Elements	84095	131605	210752

3.7.2 Grid Generation for IWT Ice Shapes

The MCCS is used to numerically determine the aerodynamic performance of the IWT ice shapes. Due to the fact that the ice geometry contains extremely complex contours, a much finer mesh is required than for the clean airfoil performance. The mesh settings for the far field edge are kept and are represented in Table 3.5. The mesh around the ice geometry is adjusted for the glaze, mixed, and rime ice, depending on the case. The resulting grids are represented in Figure 3.13

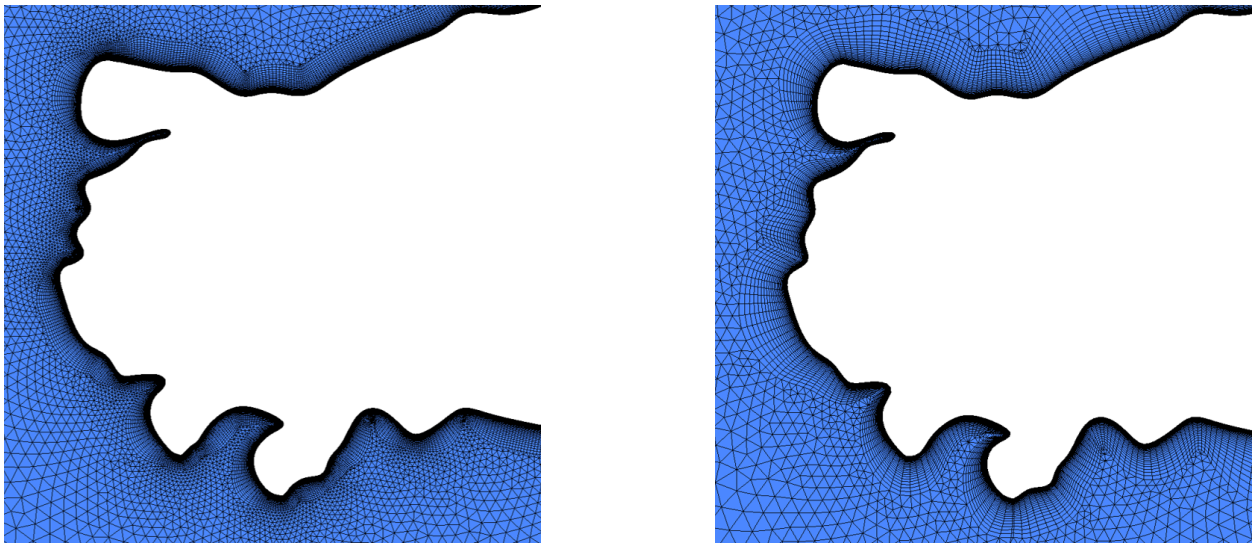

(a) (b)

Figure 3.12: (a) Grid fine, (b) Grid coarse

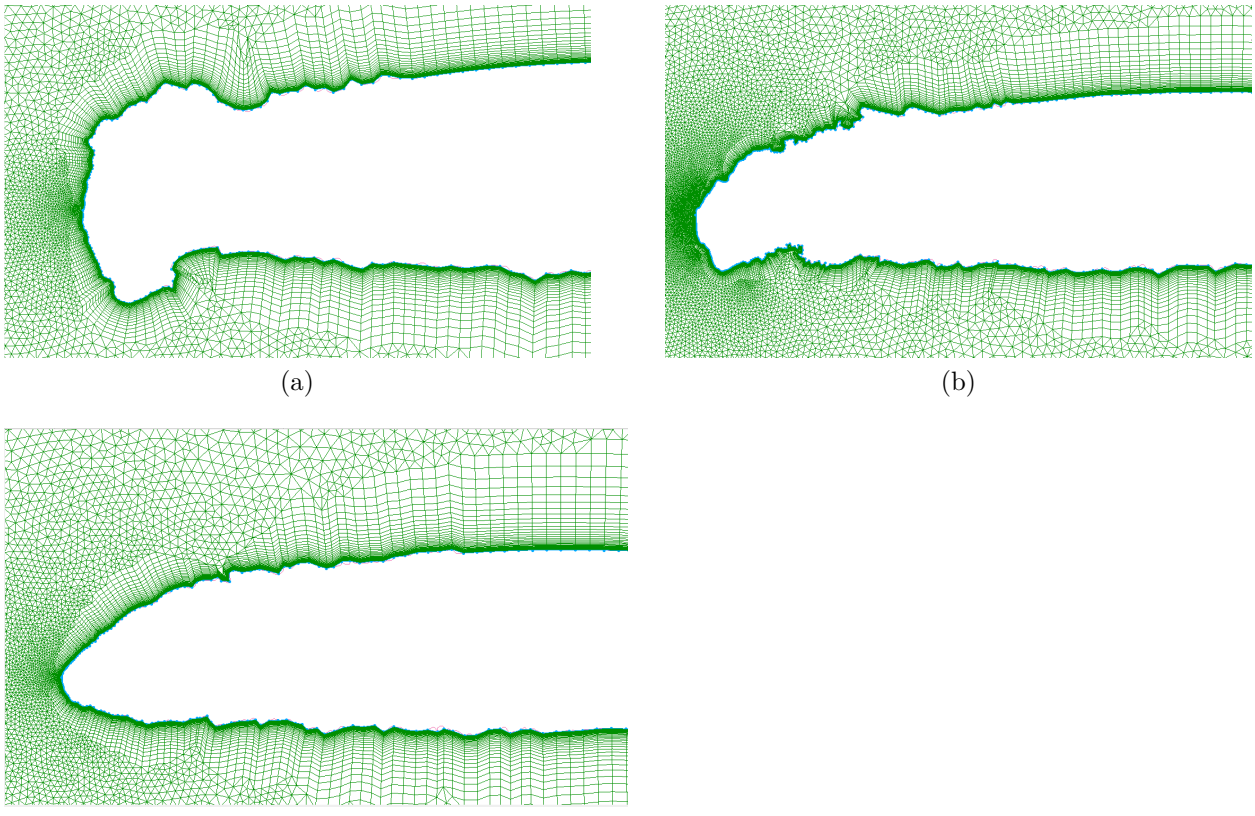

(a) (b)

(c)

Figure 3.13: Grid of a MCCS of digitized IWT results of a (a) glaze ice geometry at −2 °C, (b) mixed ice geometry at −4 °C, (c) rime ice geometry at −10 °C

4 Results

4.1 Geometry of Skywalker X8

General design and surface deviation
The result of the reverse-engineered 3D model is shown in figure Figure 4.1. Picture (d) in the same figure shows the reconstructed model and the scan placed at the same position. Pink represents the reconstructed surface, green and yellow the wing and the fuselage of the scan, respectively. The main deviations are visible at the nose section of the fuselage, the wing root and the TE.

Figure 4.1 (a) shows the curvature distribution of the surface for the scanned model and the reverse-engineered surface model. The colors represent isolines of equal curvature. In average the scan shows a continuous distribution of the curvature for both, the wing and the fuselage. They merge into each other except for a small discontinuity at the separation surface. However, the curvature has much noise since it is only G1 continuous. There is also a change in curvature on the control surfaces. It can be assumed that these are designed with an independent profile. The service cover to the payload bay is located on the top of the fuselage. This is not precisely aligned in the scan. Therefore, it has a different curvature in relation to the surrounding fuselage surfaces. This is corrected in the design process. Therefore, a deviation from the scan is shown in this area. The reconstructed surface, on the other hand, is almost completely G2-continuous, which is reflected in a significantly more uniform curvature distribution. The only exceptions are at the interface between wing and fuselage and in the rear middle fuselage area. Significant deviations in comparison to the scan are in the already mentioned rear middle fuselage area. On the wing there are slight deviations in the middle of the wing and on the control surfaces, as they are designed together with the airfoil profile.

Resulting IWT X8-664 airfoil deviation and curvature analysis
In Figure 4.2 (b) and (c), the wing profile resulting from the wing reconstruction is shown in blue, and the section of the scan in red. These are both located at the representative center section examined in IWT at the spanwise position $Y = 664$ mm. There is a good match between the two sections. In addition, a curvature analysis shows the smooth curvature across the upper and lower surfaces.

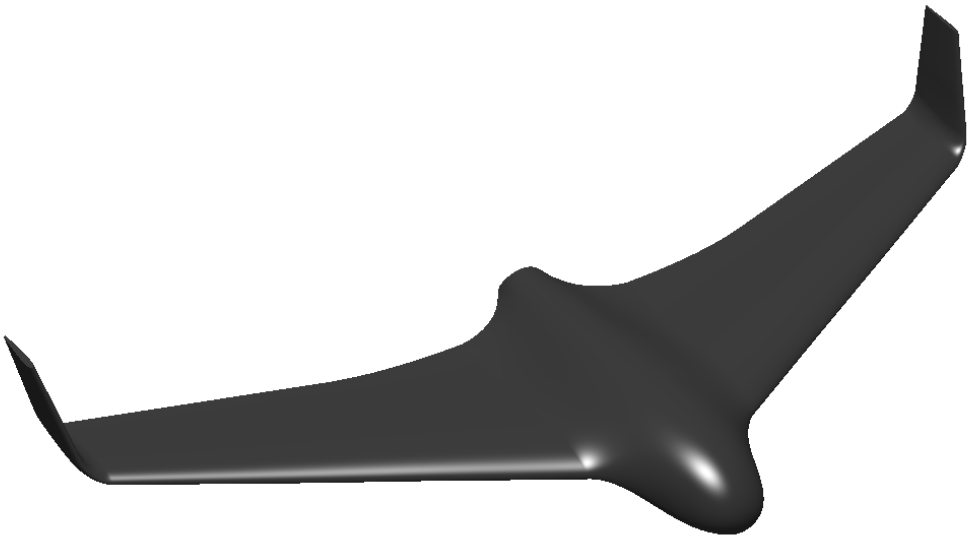

(a)

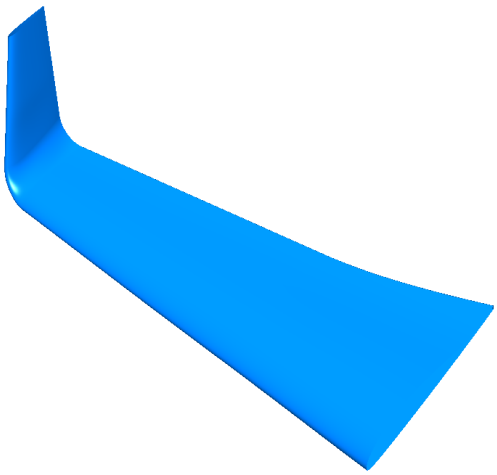

(b)

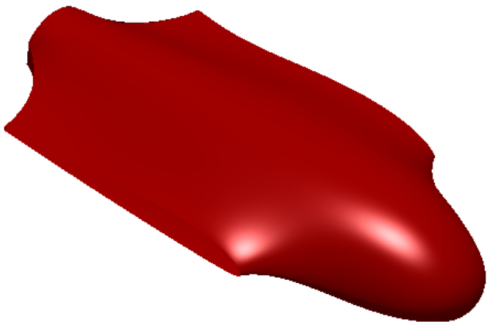

(c)

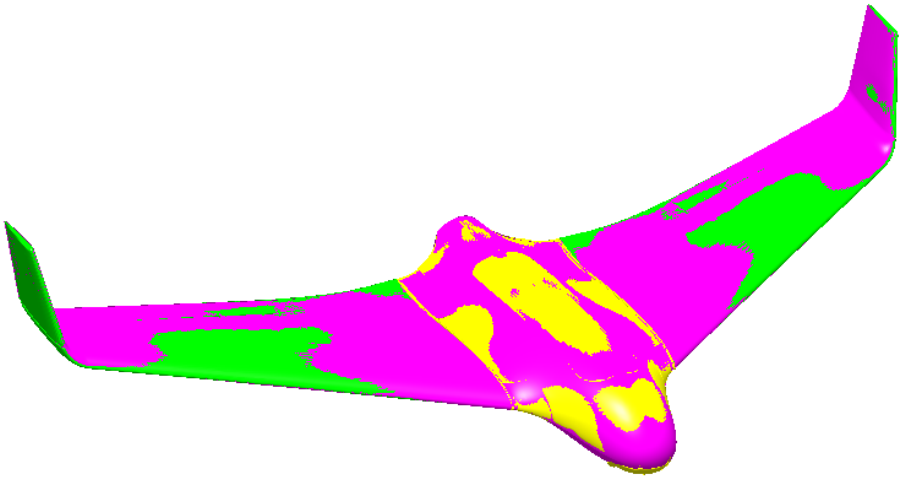

(d)

Figure 4.1: (a) Reverse-engineered Skywalker X8, (b) Wing, (c) Fuselage, (d) Surface deviation analysis

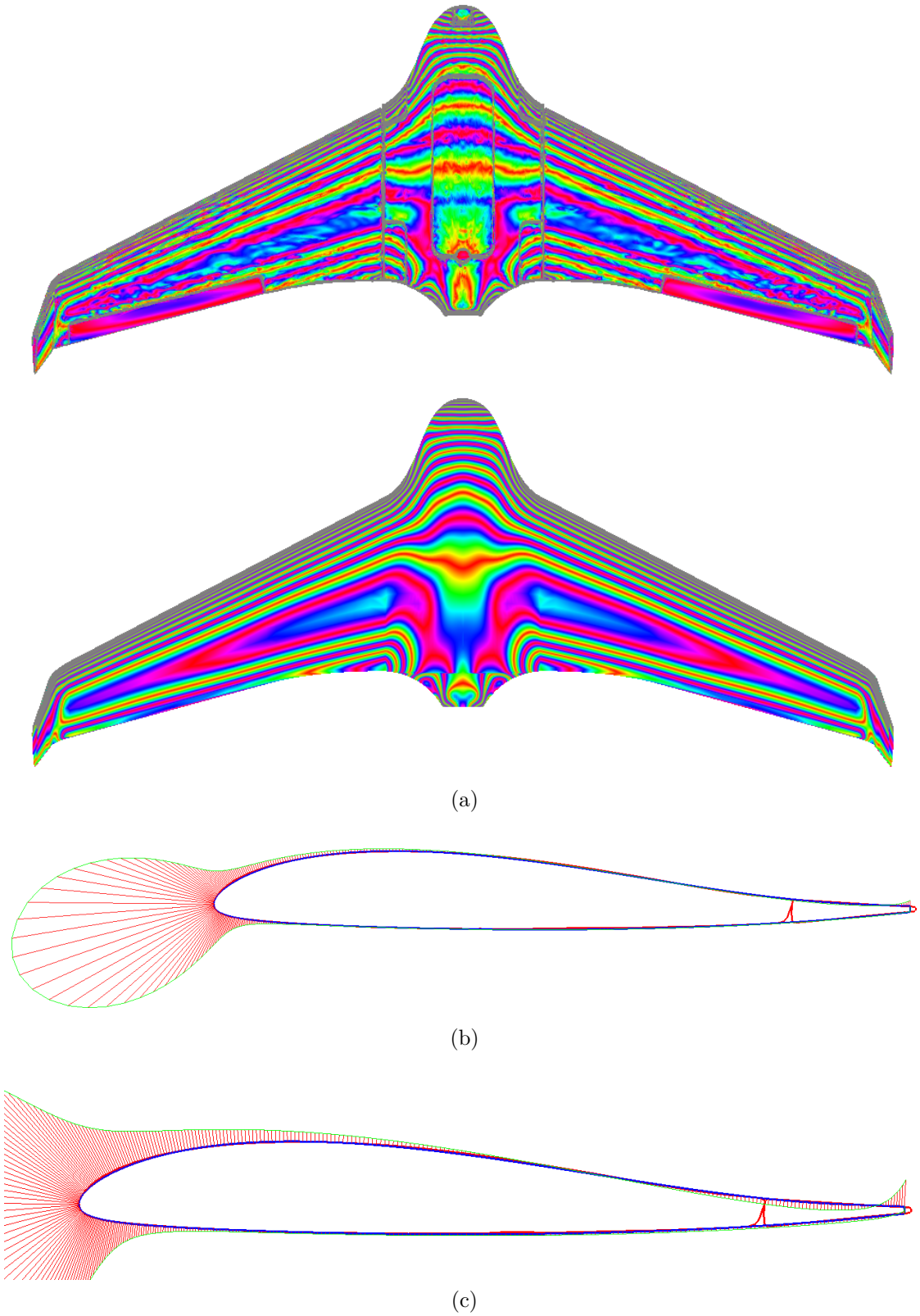

Figure 4.2: (a) Surface curvature, (b) Curvature of X8-664 airfoil (c) Curvature of X8-664 airfoil detailed

4.2 Grid Convergence Study S5010

Figure 4.3 shows the result of the grid convergence at an AoA of $\alpha = 4°$ with the S5010 reference airfoil. The grid convergence study shows a non-monotonous behavior for the lift- and pitch moment coefficient for the refined grids. In order to use the Richardson extrapolation or the GCI-method, the property has to converge monotonously. That is only fulfilled by the drag coefficient. For this, a 7^{th} order of convergence is found. The GCI for the coarse and the fine grid is less than 1 %. The numeric exact value is calculated to 0.01077 and plotted at $h = 0$. For the lift and drag coefficient, the relative error ϵ is used, even though neither the refinement factor nor the order of convergence is taken into account in this error. According to Slater [29], that might lead to an underestimation or overestimation of the error and need further interpretation. For the lift coefficient, the relative error is small for all grids with less than 0.26 %, and the changes in the values seem to be insignificant for the application of icing. The relative error for the momentum coefficient is quite significant with −38.5 %. However, the values are three orders of magnitude lower than the values for the lift coefficient. Therefore, the relative error becomes more significant. The values for the grid convergence study are summarized in Table 4.1.

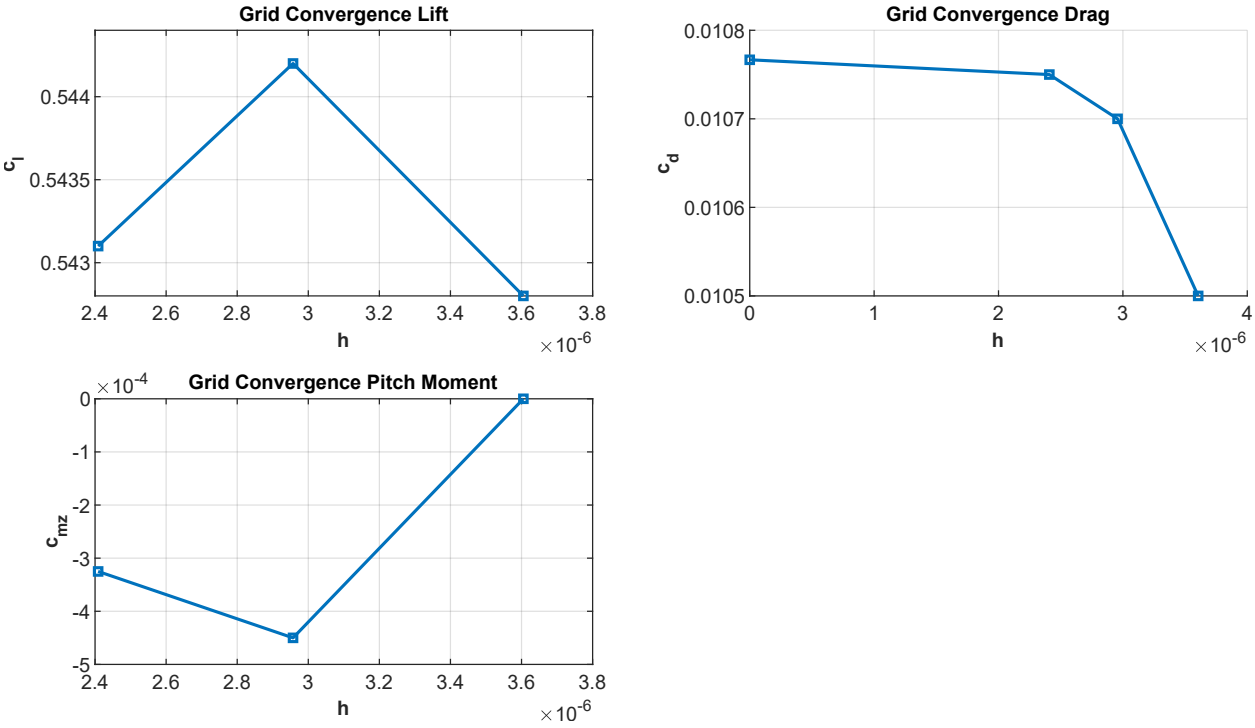

Figure 4.3: Grid convergence study S5010 at $Re = 300000$ and $\alpha = 4°$

Furthermore, the grid convergence is extended to a sweep analysis from $\alpha = -2°$ to $\alpha = 13°$ to investigate the influence of the grid for the range of AoA until stall occurs. This is shown in Figure 4.4. The course of the curves for the drag- and lift coefficients in the non- stall region are similar for all grids. At AoA higher than $\alpha = 10°$ the course mesh predicts a higher drag. For the pitch moment coefficient, the hinge point in this study is located at

Table 4.1: Grid convergence study S5010 at $Re = 300000$ and $\alpha = 4°$

Parameter	$\mathbf{c_l}$	$\mathbf{c_d}$	$\mathbf{c_{mz}}$
p	–	7.0	–
ϵ_{coarse}	0.26%	1.9%	100%
ϵ_{fine}	−0.20%	0.47%	−38.5%
GCI_{coarse}	–	0.78%	–
GCI_{fine}	–	0.19%	–
$c_{d,exact}$	–	0.01077	–

the LE. While the fine and medium grids are a almost equal for the whole range, the coarse mesh deviates for AoA below $\alpha = 6°$ with a maximum at $\alpha = 1°$ and for higher AoA than $\alpha = 10°$.
Based on the results of the two studies, the medium is used for the clean airfoil performance, because all grids show a similar behavior with respect to lift and drag. But while the coarse grid is deviating for the pitch moment coefficient at lower AoA, the fine mesh does not improve the results. Therefore, the medium grid is the best compromise between accuracy and calculation effort.

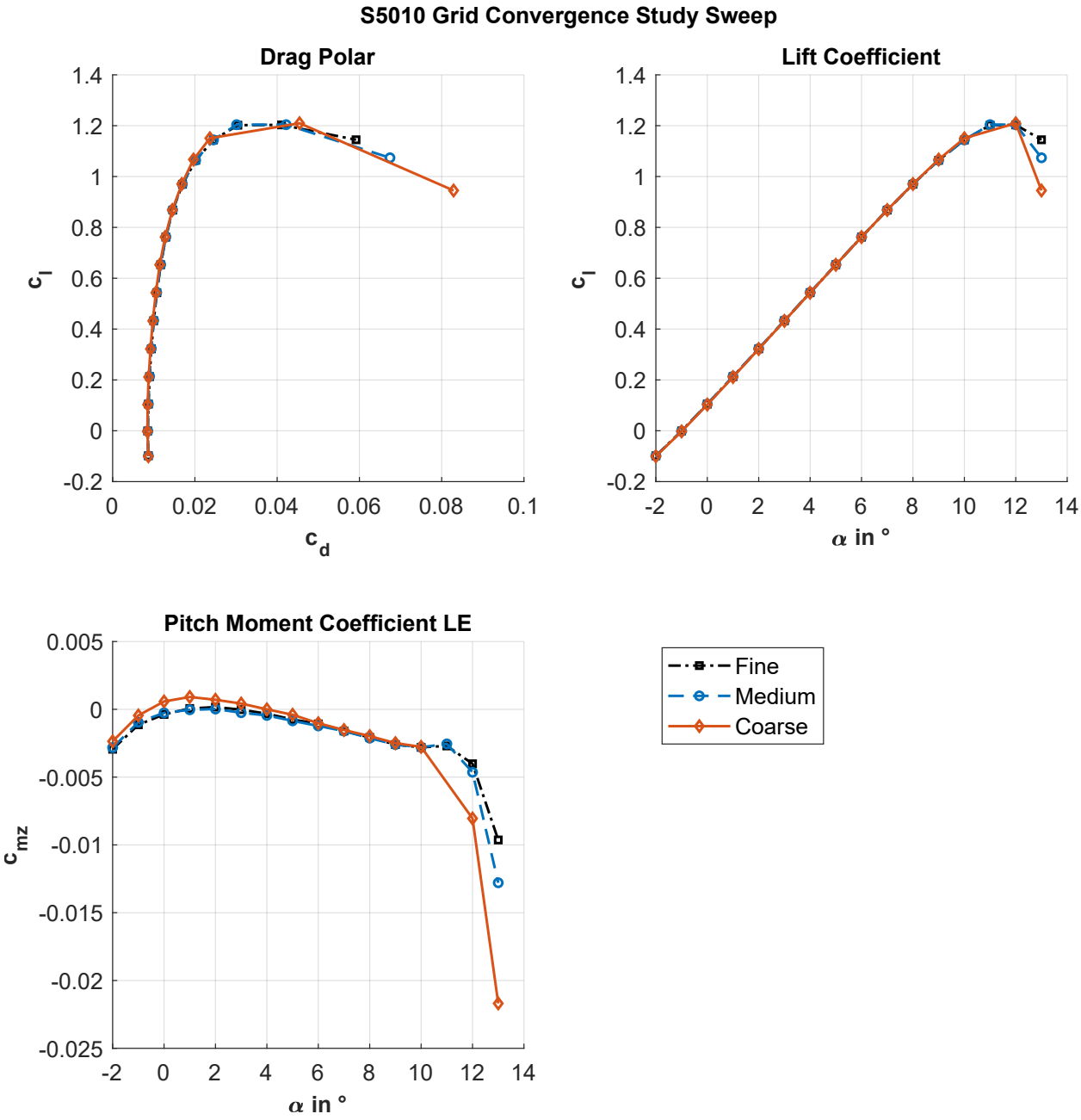

Figure 4.4: Grid convergence study sweep analysis of S5010 at $Re = 300000$ and $\alpha = 4°$

4.3 Clean Airfoil Performance

The clean airfoil performance is the first step in analyzing the performance degradation. As described in Section 3.3, the validation of the clean airfoil performance model is done with the reference profile S5010 and repeated with the X8-664 airfoil.

4.3.1 S5010

The results calculated by FENSAP are compared to XFLR5 and wind tunnel data by [31] et al. Two different Reynolds numbers are investigated since the maximal Reynolds number by Selig et al. is $Re = 300000$, but the in-flight Reynolds number of the Skywalker- X8 is approximately $Re = 550000$. Furthermore, the influence of the drag regarding the pitch moment is investigated. The results for the drag- lift and pitch moment coefficients of the S5010 airfoil are presented in Figure 4.5.

Analysis of Re = 300000
Drag coefficient
While the results of Selig at el. and FENSAP match closely for the drag, XFLR5 predicts a 17.38 % lower drag at a AoA of $\alpha = 4°$. This offset is almost constant for a range from $\alpha = 0°$- $\alpha = 9°$. Since the $Re = 300000$ case is calculated twice in FENSAP with the same model setup besides the hinge point for the pitch moment, the results are expected to be the same. The difference in the drag and lift for $\alpha = 13°$ is due to incomplete convergence. To reduce the influence of small fluctuation in the last iterations, a mean value is calculated by averaging the last 5 % of the performed iterations. But the fluctuations for high AoA are to large to be compensated. The results are nevertheless displayed in order to recognize the stall angle.

Lift coefficient
The lift coefficients for the numerical solutions from XFLR5 and FENSAP are similar in terms of the lift gradient, the stall angle, and the zero lift angle. The measured value at $\alpha = 1°$ of Selig et al. is approximately 30 % and at $\alpha = 9°$ approximately 12 % smaller compared to the numerical solution. The difference in zero lift angle is approximately $\Delta\alpha = 0.7°$. Since no values above $\alpha = 11°$ are available, this is assumed to be the stall angle, which matches the numerical solutions.

Pitch Moment coefficient
The pitch moment coefficient shows an increasing difference by using the LE- point or the $c/4$- point as the hinge point. The moment around the LE- point is converted to the $c/4$- point by only taking the lift into account. The relation is given by Equation (4.1).

$$c_{m,c/4} = c_{LE} + \frac{c_l}{4} \tag{4.1}$$

For small AoA from $\alpha = -2°$ to $\alpha = 3°$ there is no significant difference in the methods. But for increasing AoA the drag component gains importance. While the LE- method

diverges from the XFLR5 solution, the $c/4$- point method converges to the XFLR5 solution. Therefore the pitch moment with the hinge point at the $c/4$- point is used in this work. In addition, there is a significant deviation in the pitch moment. While the XFLR5 solution has a monotonically decreasing trend from $\alpha = 0°$ to approximately $\alpha = 9°$, the FENSAP solution shows an increasing trend from $\alpha = -2°$ to $\alpha = 0°$, followed by an approximately constant value up to $\alpha = 3°$ and only for AoAs greater than $\alpha = 3°$ the gradient becomes negative.

Analysis of Re = 550000
Since the Reynolds number for the X8-664 examined later is approximately $Re = 550000$, this case is also examined with the S5010 profile. The drag coefficient for the higher Reynolds number is slightly lower compared to $Re = 300000$. The results for the pitching moment between $Re = 300000$ and $Re = 550000$ change significantly less in XFLR5 than in FENSAP, or rather the FENSAP solution approaches the XFLR5 solution for the higher Reynolds number.

Pressure distribution
There are some deviations between XFLR5 and FENSAP, so further investigations are conducted based on the pressure distribution. In the comparison between FENSAP and XFLR5, the latter shows an earlier laminar-turbulent transition at the top of the profile and higher pressure in TE- area. For the higher Reynolds number, the transition point shifts in both FENSAP and XFLR5 into the direction of LE.

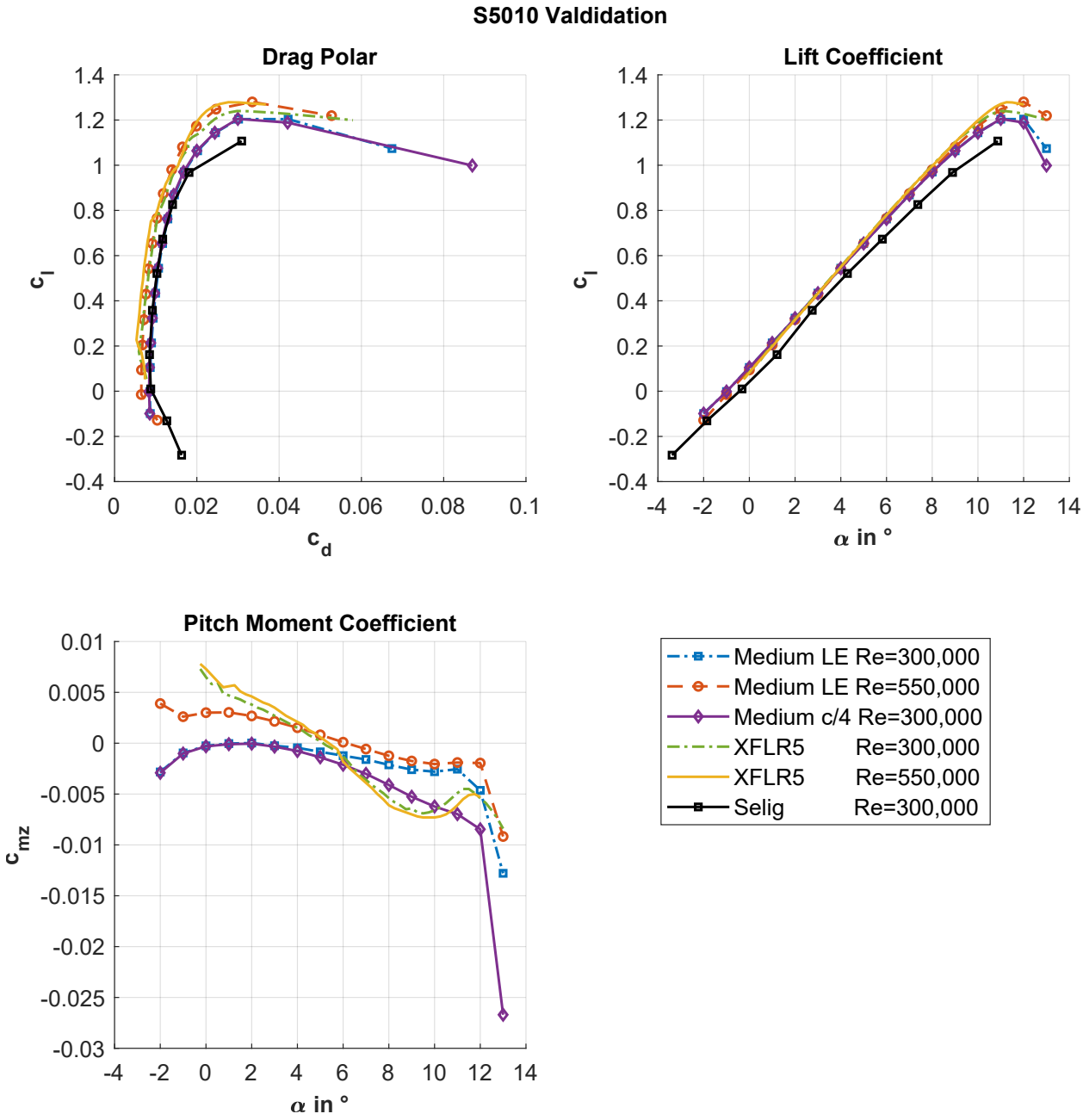

Figure 4.5: S5010 validation with XFLR5 and wind tunnel data by Selig et al. [31]

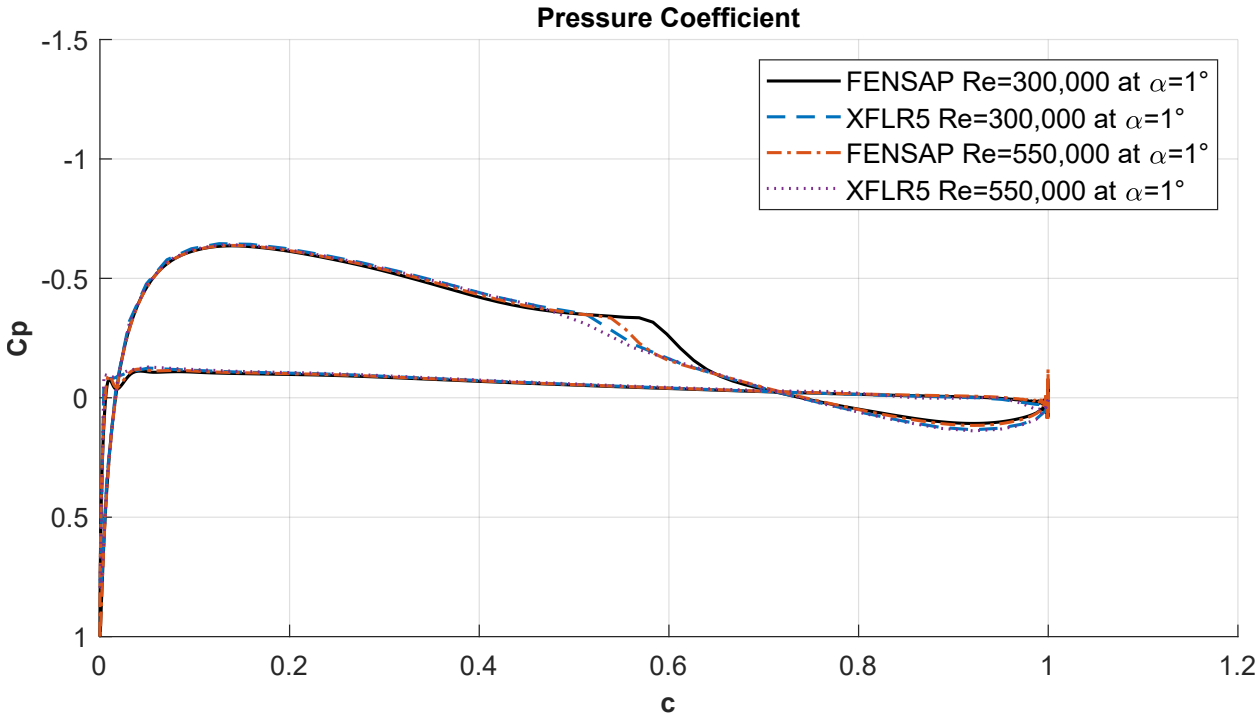

Figure 4.6: S5010 pressure coefficient at $\alpha = 1°$

4.3.2 X8-664

The aerodynamic performance of the reverse-engineered Skywalker X8-664 airfoil is shown in Figure 4.7. Analogous to the reference profile S5010, the results of the FENSAP solution are compared with XFLR5. Although the investigated IWT tests were carried out at a Reynolds number of $Re = 550000$, the Reynolds number of $Re = 300000$ is also investigated for the X8-664 to prove the plausibility of the results.

Drag coefficient
As with the S5010, the X8-664 profile also shows that XFLR5 predicts a lower resistance coefficient. At an AoA of 4° the difference is approximately 25 % at a Reynolds number of $Re = 300000$. For the relevant Reynolds number of $Re \approx 555,000$, the difference is slightly smaller at around 14 %.

Lift coefficient
In general, the lift polars of XFLR5 and FENSAP are similar and show an equal stall angle. Minimal differences are shown for the lift gradient, where XFLR5 calculates a slightly higher value, which results in a minimally higher maximum lift coefficient. This effect is seen in both investigated Reynolds numbers. In the range of about $\alpha = 1°$, the polars of the XFLR5 solution bend slightly, resulting in a slightly higher zero lift angle compared to the FENSAP solutions.

Pitch moment coefficient
The pitch moment coefficient is positive, which means the airfoil has a pitch-up moment. It has the same gradient tendency in all cases. From $-2°$ to $1°$, a negative gradient is shown for the FENSAP solution for $Re = 550000$. From $-1°$, the gradient changes rapidly to positive up to 4°, where it reaches a local maximum. For higher AoA, the pitch moment coefficient decreases until its stall angle. The difference in absolute values between XFLR5 and FENSAP is relatively high below 1°.

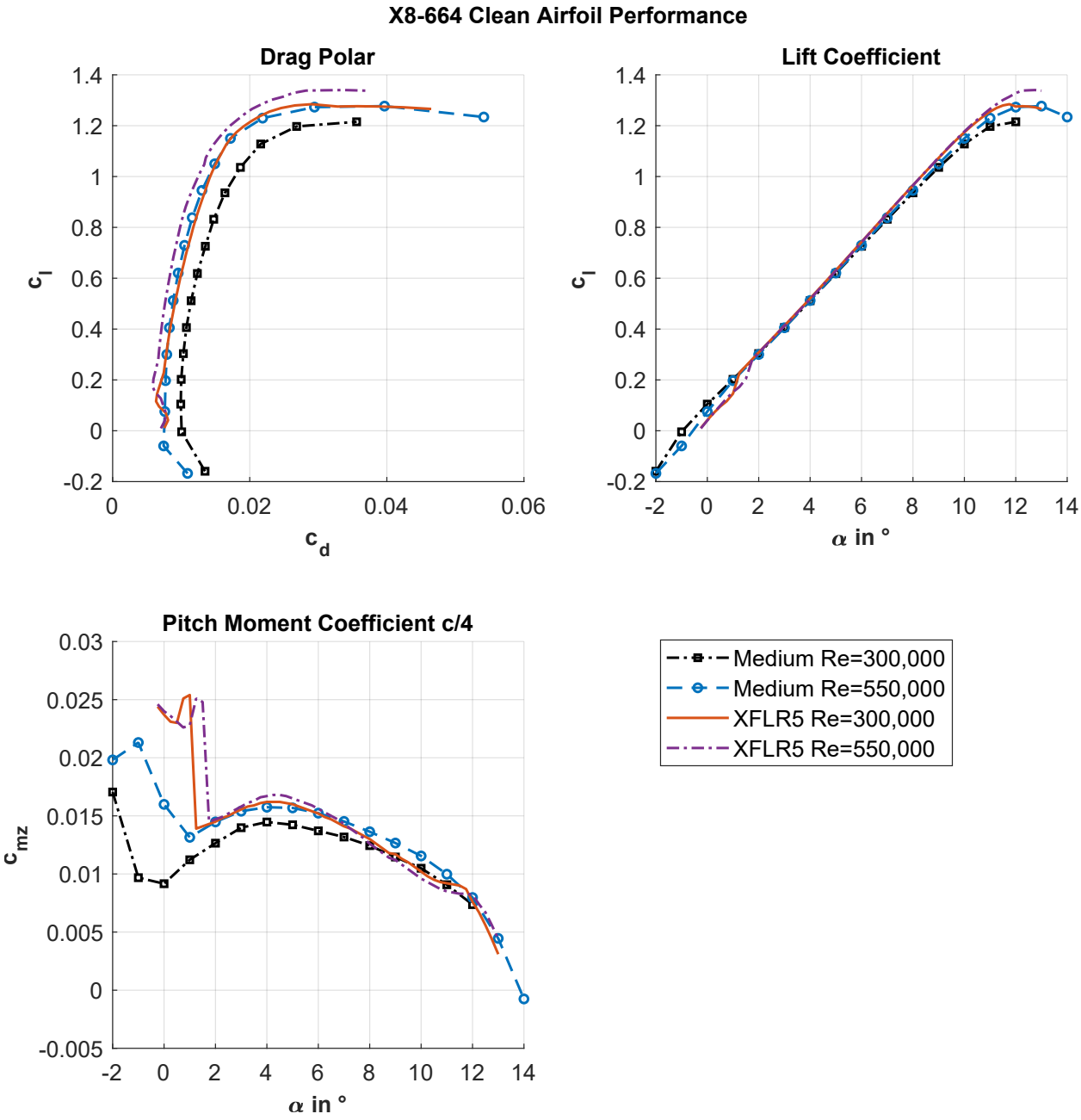

Figure 4.7: X8-664 validation with XFLR5

4.4 Ice Accretion

The second step in analyzing the performance degradation is ice accretion. Three different temperatures for glaze ice, mixed ice, and rime ice are investigated and compared to IWT results. Since a suitable numerical setup for the mixed ice regime has yet to be found, this case is considered in more detail. The results are presented in Figure 4.8. The wing section tested in the IWT has a width of $Y = 150$ mm. The representative cross-section is located in the middle at 75 mm and corresponds to the span wise position of $Y = 664$ mm on the 3D wing. The AoA is $\alpha = 4°$. The area of the cross-section of the MCCS is always larger than the local one because it is the hull curve of multiple cross-sections. The difference between these approaches is much more pronounced in the glaze ice case than in the rime ice case. This is due to stronger 3D effects in the glaze ice case. The difference in the mixed ice case is between glaze and rime ice. A common feature of all calculated ice shapes is that the volume of ice accumulation is lower than in the IWT.

Glaze ice
In the glaze ice case, a horn ice-like structure is formed in both the calculated and the IWT case. The formation of sharp horns on the top and bottom surface may be recognizable in the 75 mm cross-section in the glaze ice case. However, for the top surface horn, it is not clear from this illustration whether this is a randomly occurring event in this cross-section or a global phenomenon that is averaged out in the MCCS. The bottom horn is still recognizable at the MCCS. The calculated ice shape shows the same kind of horns and their height is approximately the same like in the 75 mm cut, but the ice shape is less developed in the flow direction. In the simulated case one larger horn at the bottom surface has formed further downstream than in the IWT. On the top surface the horn is formed more upstream compared to the MCCS.

Rime ice
As expected, an ice geometry forms in the direction of flow in the rime ice case. The difference between the local section and the MCCS hull is small. In this case the calculated ice shape is smaller than the IWT measurement too. The feathers that arise under rime ice conditions are not represented in the simulation.

Mixed ice
In the mixed ice case, a combination of rime ice and glaze is measured in the IWT. While the local cut of the top surface shows more 3D effects, the averaged MCCS section is more streamlined. The bottom surface has a significant angle in the positive y-direction, which looks like a blunt horn. Additionally, both the MCCS and the 75 mm cut show feather-like structures at the bottom surface. For the calculated ice shapes, a time-step study is performed, and the influence of the density model is investigated. The constant density model predicts significantly too less accumulated ice. The general shape of the top surface is more streamlined compared to the IWT results. The horn at the bottom surface shows a similar angle. A phenomenon that cannot be observed in the IWT is the dent in the

area of the stagnation point. The time-step study with the constant density model shows a smoother surface for more time steps, and the angle of the lower horn becomes more obtuse and diverges from the IWT results. The impact density model is a beta function in FENSAP. Therefore, it is tested to see if it provides suitable results yet. Two different time steps are investigated, but no convergence is achieved by double the number of time steps. The general ice shape shows a more pronounced horn ice structure compared to the IWT results. On the top surface, the ice accretion is much more upstream compared to the MCCS shape but similar to the local cut. 3D effects are not taken into account on the top surface, but there are some feather- like structures on the bottom surface.

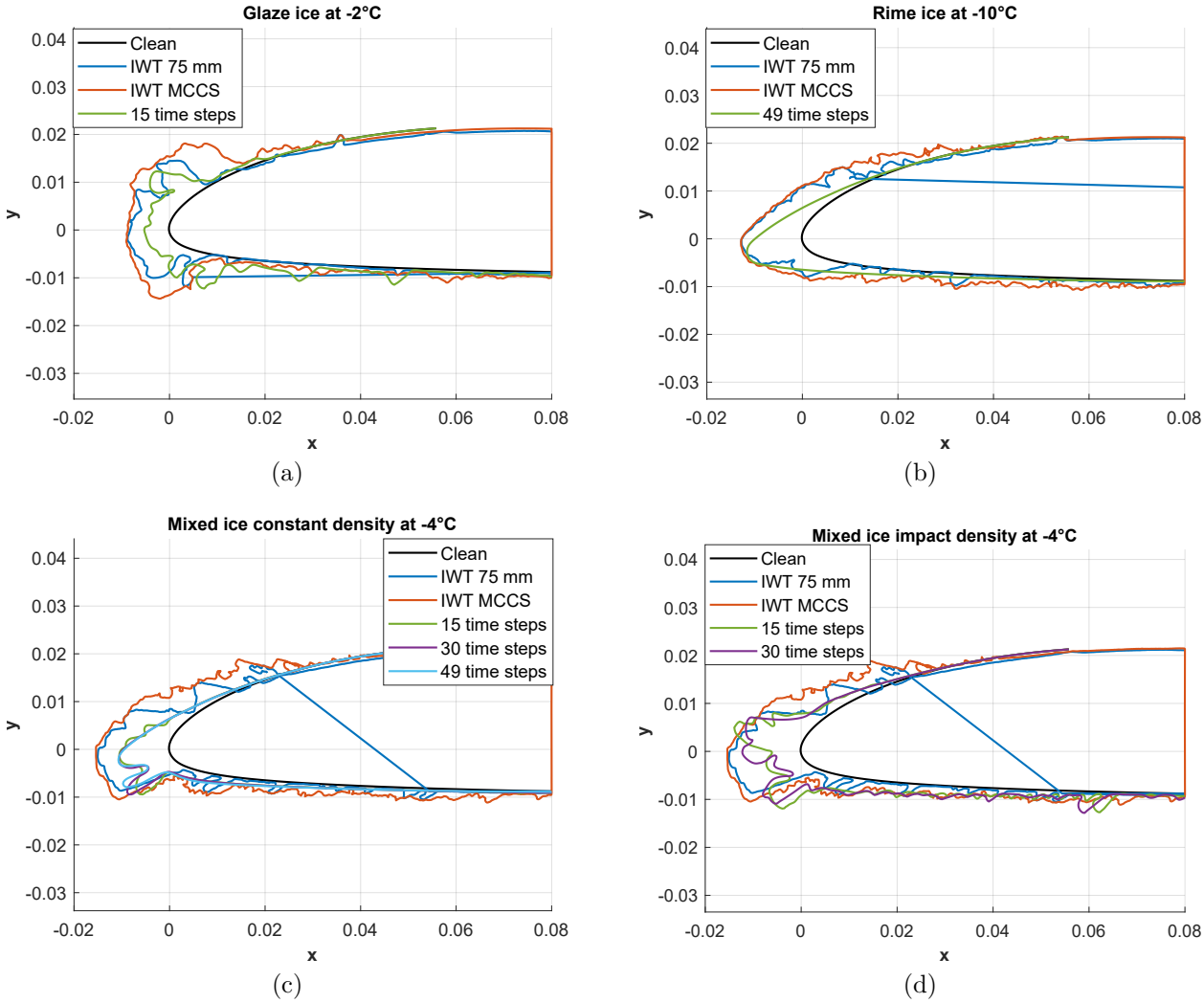

(a) (b) (c) (d)

Figure 4.8: (a) Validation for glaze ice (b) Validation rime ice (c) Validation for mixed ice with constant density setting (d) Validation for mixed ice with impact ice density setting

4.5 Iced Airfoil Performance

The iced airfoil performance is the last step in evaluating performance degradation. Again, the drag-lift- and moment coefficients are analyzed. In addition, the stall angle is also considered, as this is crucial for the safe operation of the UAV. The analysis is divided into three different steps. At first, a grid convergence study is performed at an AoA of $\alpha = 4°$. The second analysis is about the comparison between the calculated ice shapes, the clean airfoil, and the MCCS of the IWT tests. It analyzed for each ice regime separately. In the third analysis are the different ice regimes compared to each other using the IWT measurements.

4.5.1 Grid Convergence Iced Airfoil Performance

Figure 4.9 shows the result of the grid convergence for the iced performance for the glaze ice case at an AoA of $\alpha = 4°$ with the X8-664 airfoil. That case was selected due to the most complex geometry. The grid convergence study shows a monotonous behavior for all coefficients. Therefore, the Richardson extrapolation and the GCI-method were conducted. The numeric exact value is plotted at $h = 0$. For the drag, a 2.62^{th} order of convergence is found. The coarse GCI value is just slightly above 1 % und is reduced for the fine GCI value to 0.32 %. The numeric exact value is calculated to be 0.0451. The lift coefficient shows a slightly lower order of convergence with 1.87. Both GCI values are below 1 %. The numeric exact value is calculated to be 0.442. The best convergence is achieved with the moment coefficient. The convergence order is 5.49. Already, the coarse GCI value is less than 1 % and is reduced even further according to the convergence order. The exact value is calculated to be 0.0212. The values for the iced performance grid convergence study are summarized in Table 4.2.

Table 4.2: X8-664 iced performance grid convergence sweep for glaze ice at -2 and $\alpha = 4°$

Parameter	c_l	c_d	c_{mz}
p	1.87	2.62	5.49
ϵ_coarse	0.007 %	-0.019 %	0.0556 %
ϵ_fine	0.003 %	-0.0058 %	0.0047 %
GCI_{coarse}	0.65 %	1.04 %	0.649 %
GCI_{fine}	0.28 %	0.32 %	0.006 %
f_{exact}	0.442	0.0451	0.0212

Analogous to the clean case, the iced performance grid convergence study is extended to a sweep analysis from $\alpha = -2°$ to their equal stall angle of $\alpha = 6°$. This is shown in Figure 4.10. The course of the curves for the drag- and lift coefficients in the non-stall region are similar for all grids. The course mesh predicts a slightly higher drag at AoA lower than $\alpha = 3°$ and

an appoximatly 8 % lower pitch moment coefficient between -1 ° to -3 °.

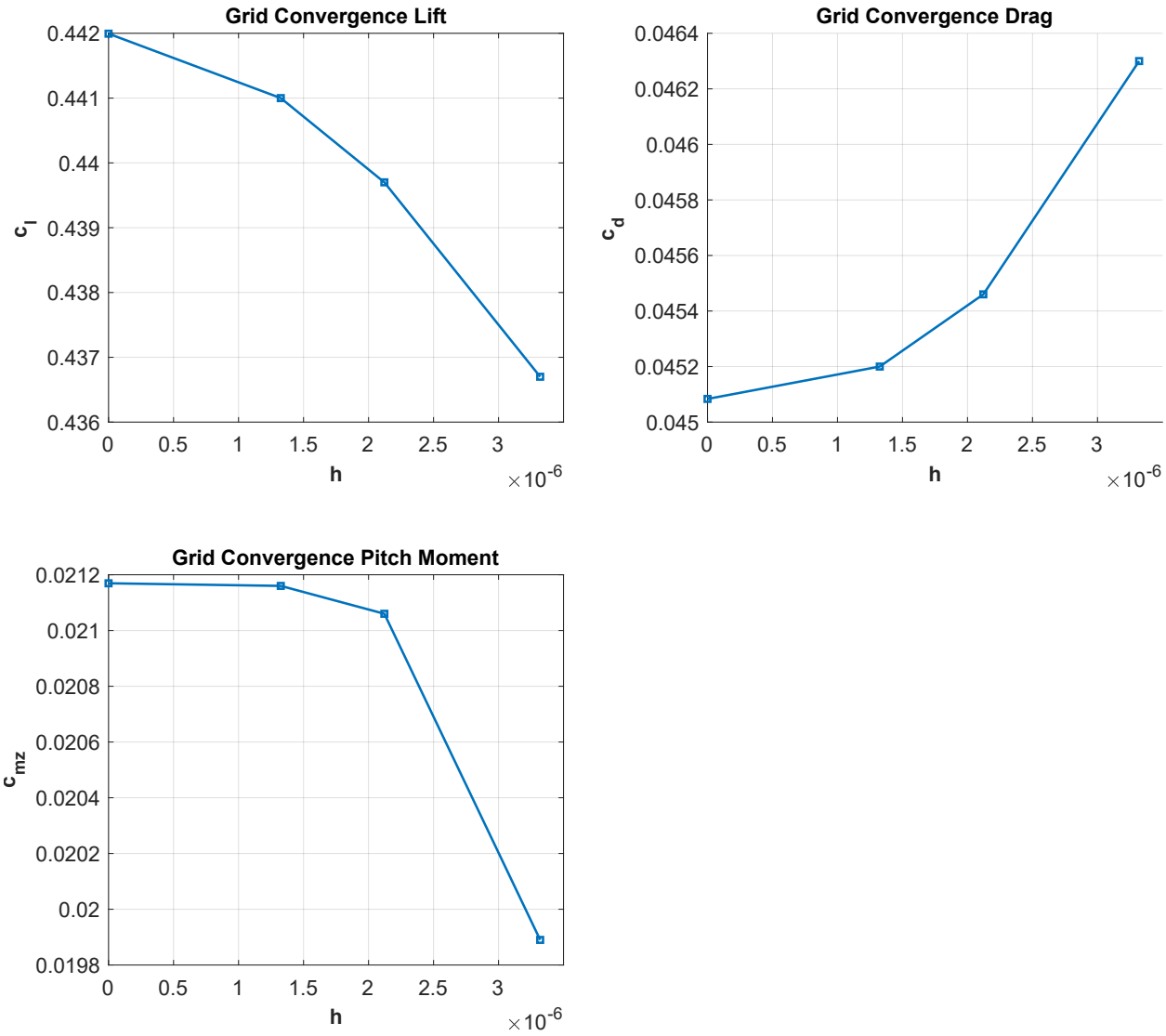

Figure 4.9: X8-664 iced performance grid convergence for glaze ice at -2 °C and $\alpha = 4°$

Based on the results of the two conducted studies and the deviation of the ice shapes between the IWT measurement and the calculated ice, the coarse grid is considered a minor effect of the aerodynamic performance. Therefore, the coarse grid is used to reduce computational costs for the iced airfoil performance. The medium grid may be considered for more detailed analysis.

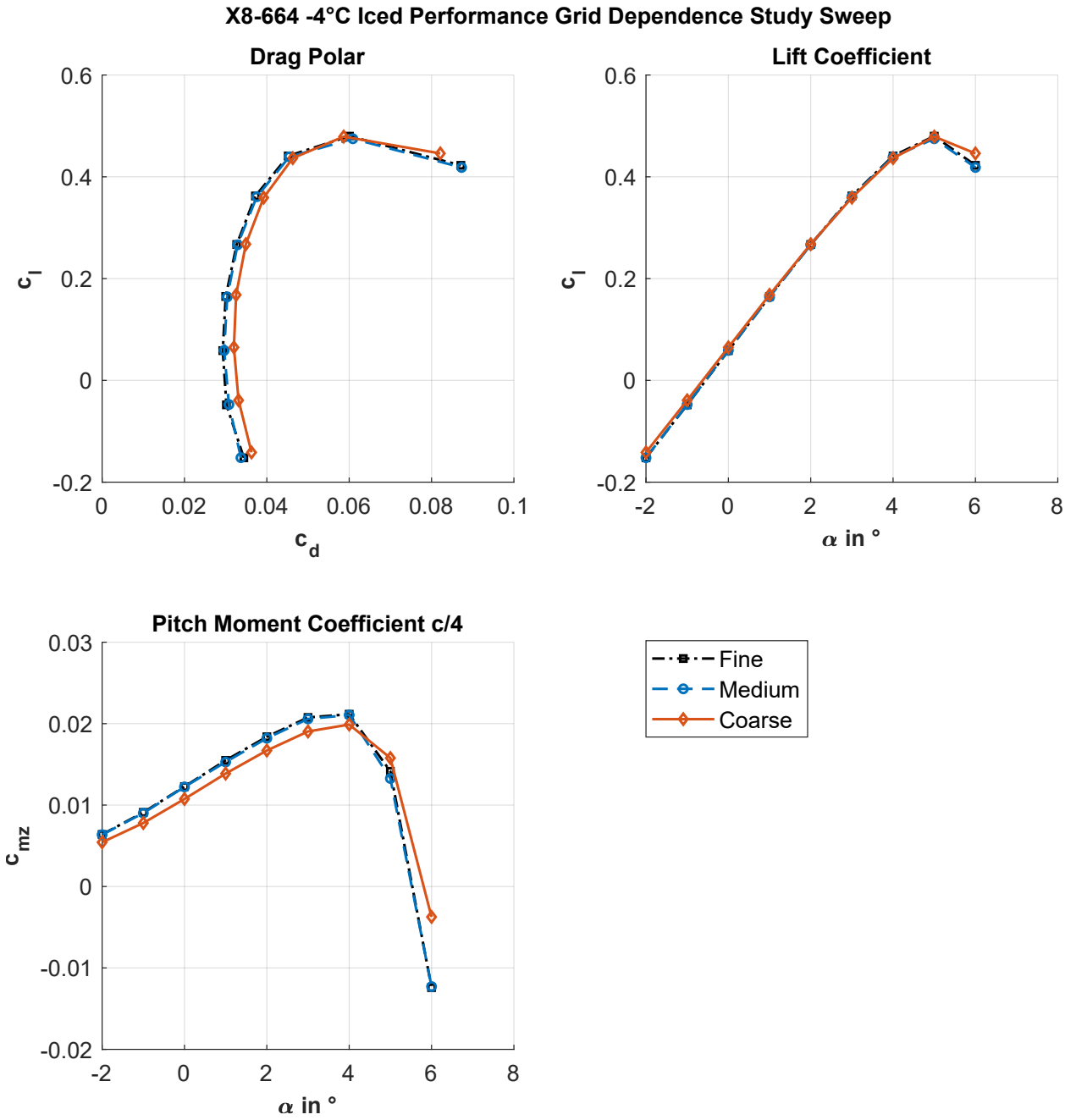

Figure 4.10: X8-664 iced performance grid convergence sweep for glaze ice at -2 °C and $\alpha = 4°$

4.5.2 Iced Airfoil Aerodynamic Performance

Glaze ice

The iced performance of the clean geometry, the MCCS, and the calculated ice shape for the the glaze ice case are shown in Figure 4.11.

Lift
There is a significant reduction in the stall angle from about $\alpha = 12°$ to about $\alpha = 5°$. The lift gradient is slightly reduced. The reduction in the stall angle reduces the maximum lift from around 1.25 to 0.45. The calculated and measured ice shapes behave similarly.

Drag
The minimum drag increases from approximately 0.007 to 0.03 for the calculated ice shape and to 0.047 for the measured ice shape. At their stall angle of 5°, the drag coefficient of the iced airfoils increases from approximately 0.009 to 0.06 compared to the clean configuration. The coefficients of the iced airfoils diverge significantly from each other in the AoA range below 3°. At $-2°$ AoA, the drag coefficient of the calculated geometry is approximately 0.035, and that of the measured geometry is approximately 0.07.

Pitch moment
The pitch moment of the iced geometries has a similar course to that of the clean airfoil in the range of 0° to 4°, but with greater gradients. The measured ice shape is slightly below and the calculated ice shape above the clean airfoil, except for 0° AoA. The two iced geometries show an opposite course between $-2°$ and 0°.

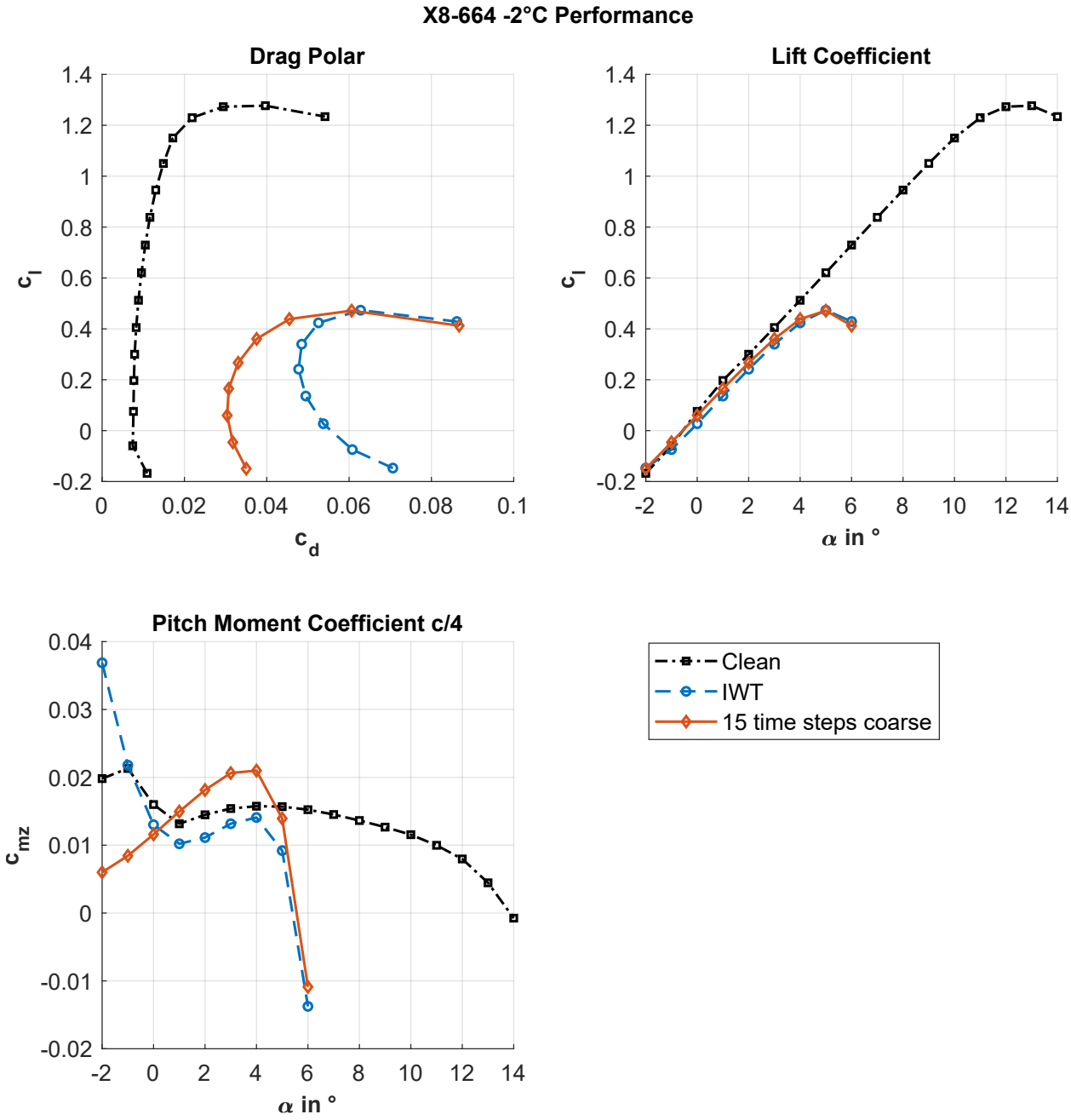

Figure 4.11: X8-664 iced performance for glaze ice at -2 °C

Mixed ice

The iced performance of the clean geometry, the MCCS, two different time steps for the constant density model, and the 30 time step impact density model are shown in Figure 4.12. For both the lift and drag as well as the pitch moment, it can be seen that the two calculated ice shapes of the constant density model behave similarly and that the performance of the impact ice model is similar to the MCCS results.

Lift coefficient
For the lift coefficient, there is a graduated reduction in the stall angle and the maximum lift coefficient. The two ice shapes of the constant density model achieve a maximum lift of 0.95 at a stall angle of approximately 10°. The IWT ice shape achieves a maximum lift of approximately 0.72 at a stall angle of 8° and the impact ice model 0.68 at 7°. The lift gradient behaves similarly for all geometries, with a slight reduction for the impact density models.

Drag coefficient
In general, there is a significant increase in the drag coefficient of the iced profiles. In particular, the IWT profile and the impact ice model show a strong increase in drag from about 1° AoA, also in comparison to the constant density models. The minimum resistance of the constant density models is about 0.021 at a AoA of 3°. That of the impact density model is approx. 0.03 at 2°. The value of the IWT geometry is slightly higher than the impact ice model with 0.032 at the same AoA.

Pitch moment coefficient
In general, the tendency of the iced profiles is to decrease the pitch moment in the top-heavy direction in the lower AoA range and to increase it in the tail-heavy direction for higher AoA. In general, the constant density models have a lower pitch moment coefficient compared to the IWT and impact ice model. The maximum value occurs for the iced profiles 1° before the stall angle. The constant density models have a maximum value of approximately 0.023 and 0.026 for 15 and 30-time steps, respectively, for IWT and impact density model with approximately 0.032.

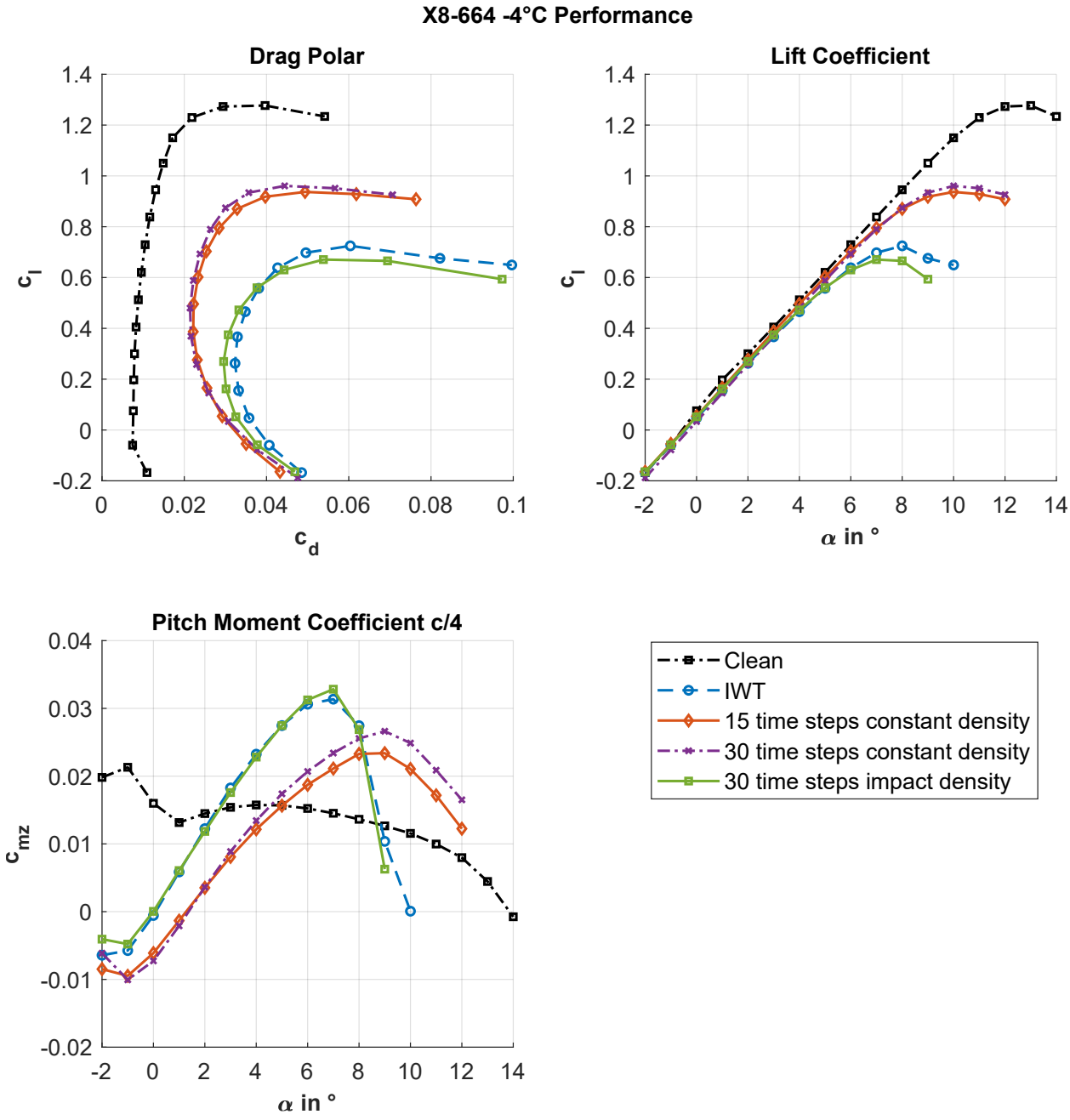

Figure 4.12: X8-664 iced performance for mixed ice at −4 °C

Rime ice

The performance of the clean geometry, the MCCS, and the calculated ice shape for the rime ice case with 49 time steps are shown in Figure 4.13.

Drag coefficient
Compared to the clean airfoil, the calculated airfoil shows an increased drag for AoA below 1° and above 7°. The IWT ice shape shows a significantly increased drag. In the region of 1° to 7°, the calculated ice shape matches the clean airfoil. The minimum drag coefficient of 0.007 is slightly higher and shifted from −1° to 1°. The IWT ice shape has a higher minimum drag of approximately 0.019 at 1°.

Lift coefficient
A reduction in the stall angle to 11° in the IWT and 10° in the calculated ice shape, respectively, is shown in **??**. The reduction in the stall angle reduces the maximum lift to 1.12 for the calculated geometry and 0.98 for the IWT. The lift gradient is similar for all cases.

Pitch moment coefficient
The pitch moment of the iced geometry shows an almost monotonous course from −2° to their respective stall angle. Both iced airfoils show an increased pitching up moment from 1° for the IWT and 3° for the calculated ice shapes. The calculated ice shape shows a small step between 0° and 1°. From then on, the two curves run at an almost constant distance of $\Delta c_{mz} = 0.007$ up to 7°. The maximum value for the IWT ice shape is approximately 0.039 at 9° and for the calculated geometry at 0.031 at 10°.

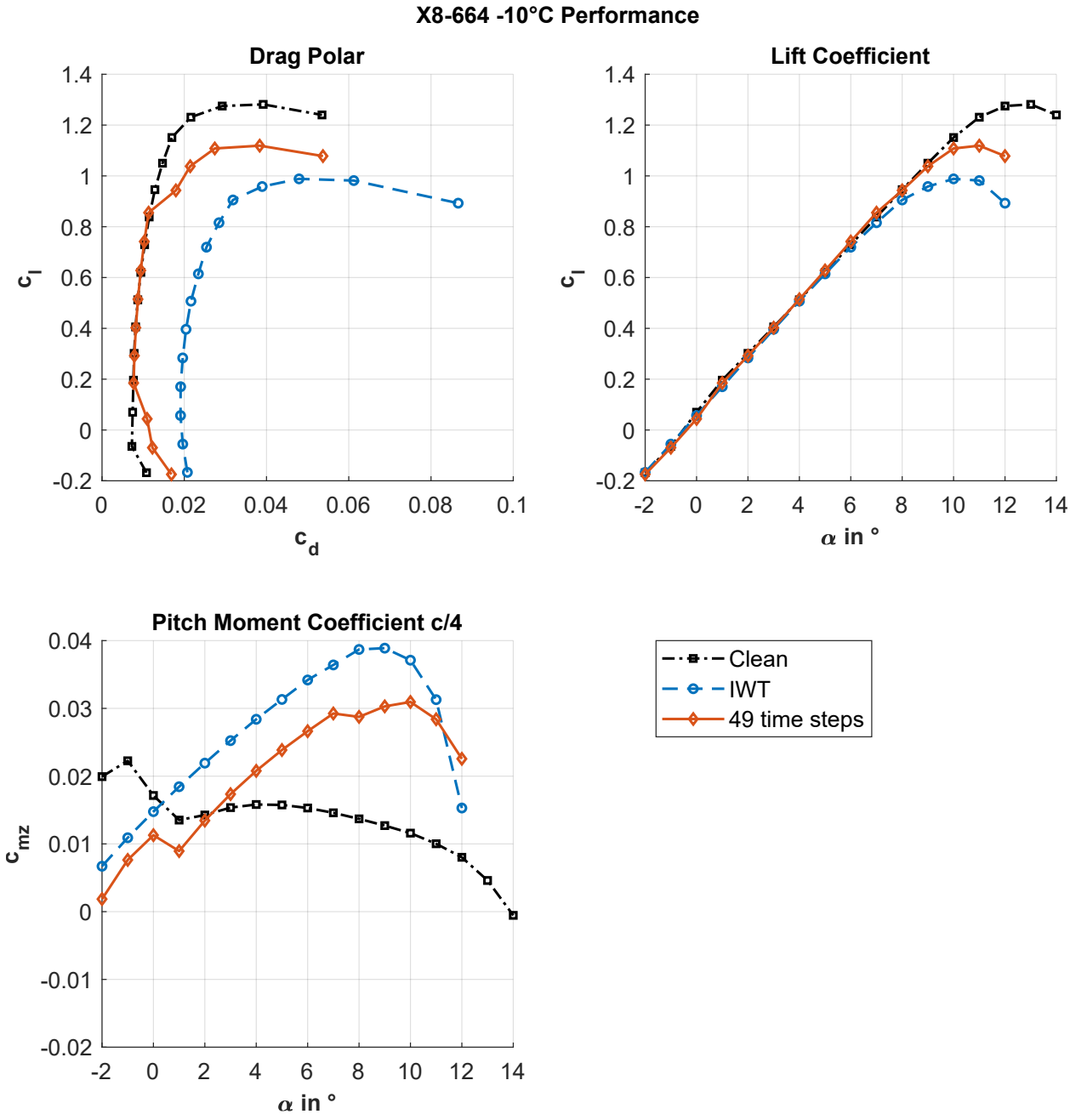

Figure 4.13: X8-664 iced performance for rime ice at −10 °C

IWT performance

After comparing the calculated ice shapes with the IWT test data, the influence on the aerodynamic performance of the individual ice regimes is examined below using the MCCS. The results are shown in Figure 4.14.

Drag coefficient
The drag coefficient increases significantly for the iced profiles. Glaze ice shows the greatest increase. Mixed ice and rime ice are in descending order between them. Not only does the minimum drag coefficient increase, but also the gradient over a change in the AoA. This results in a curve that is shifted to the right and becomes narrower.

Lift coefficient
For the lift coefficient, the stall angle is reduced from $-12°$ for the clean airfoil to 10°, 8° and 5° degrees for rime ice, mixed ice, and glaze ice, respectively. The respective maximum lift coefficients are 1.25, 0.98, 0.72, and 0.45.

Pitch moment coefficient
The iced profiles generally show a significantly greater change in the moment coefficient. While the coefficient of the clean airfoil is between about 0.021 and 0, those of the glaze ice fall are between 0.037 and -0.014, those of the mixed ice between 0.006 and 0.032 and for rime ice between 0.008 and 0.039. As already described, the curves of the iced profiles differ significantly from each other as well as from the clean airfoil geometry. While the gradient for glaze ice between $-2°$ and 1° is initially negative at a higher pitching moment, the gradients for mixed and rime ice are positive up to their respective stall angles. The mixed ice profile is the only one to show a pitching down moment between $-2°$ and 1°.

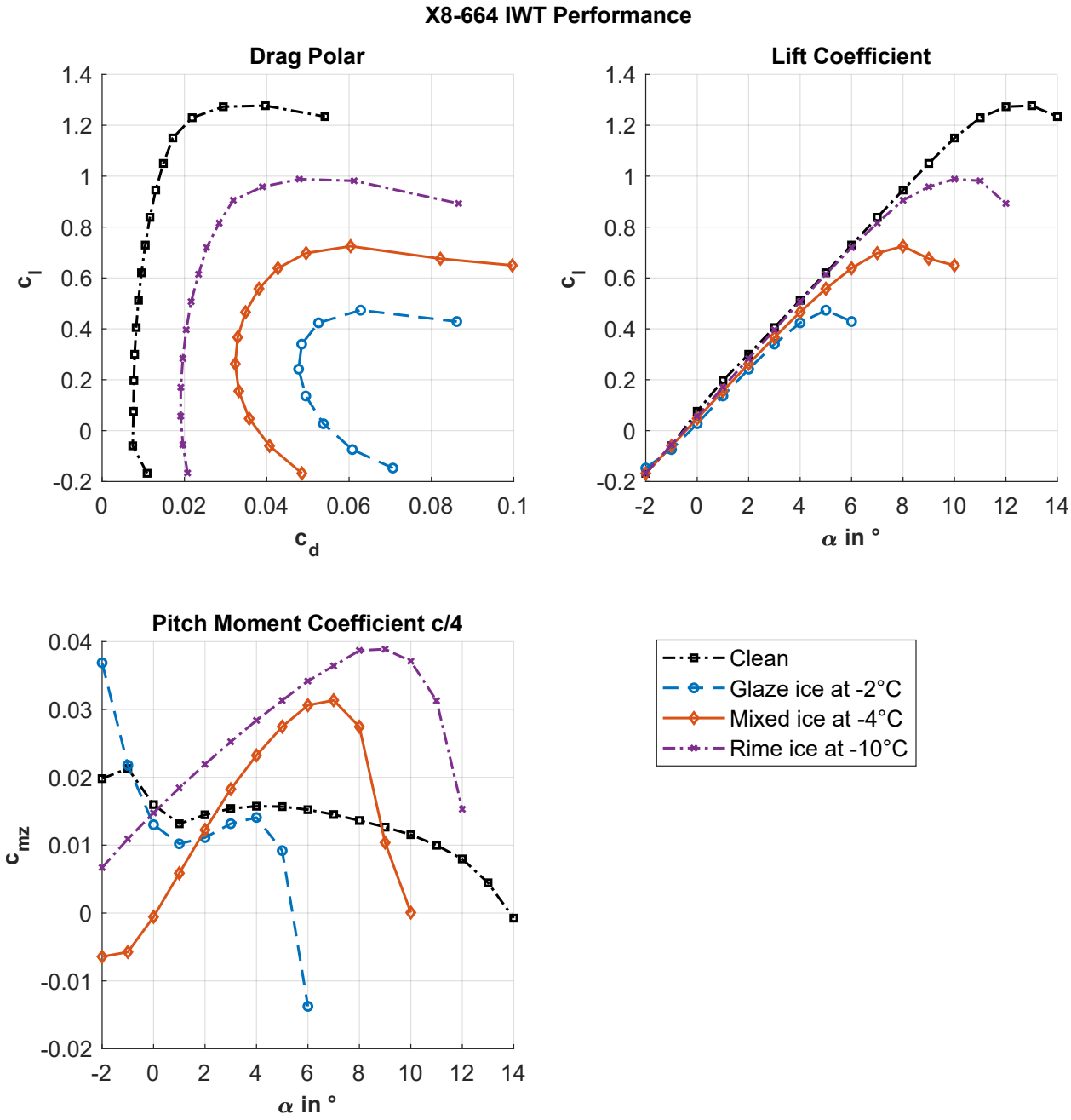

Figure 4.14: X8-664 iced performance for glaze ice, mixed ice and rime ice of the MCCS

5 Discussion

5.1 Reverse Engineering

As shown in Figure 4.1, the deviations in the 3D models of the Skywalker X8 are considered small in relation to the size of UAV, the uncertainties of the scan quality regarding the surface resolution, the alignment of the different parts and the correct scaling. Furthermore, the UAV is made of foam and thus, is vulnerable to inappropriate handling. Areas that are particularly susceptible to damage are the LE and TE. Since the scan model is provided the quality status of the drone in the scan is not known. The cross-sections from the cut wings are provided with plastic covers on both sides to protect them from damage at the interfaces. This wing is also covered with a foil. Both prevent the exact profile from being seen. For this reason, the various methods are combined with each other in order to provide the most accurate profile cuts possible for the design of the wing. Furthermore, the curvature analysis has shown that it is beneficial to use as few support profiles and guide curves as possible in order to achieve a more constant curvature distribution. However, two support profiles at the wing root and the wing tip were not sufficient for an exact approximation of the desired wing section at $Y = 664$ mm. Therefore, three airfoils are used for the wing section and two more for the winglets. The larger deviations at the wing root and at the TE are due to the construction of the wing with the outermost fuselage profile., instead of the wing root profile. Reconstructing the fuselage is a major challenge due to the complex curvature ratios. A satisfying result could only be achieved with a correspondingly high number of guide curves. The tail section of the fuselage, in particular, with its discontinuous TE curves, is not yet connected to the rest of the fuselage in a G2 continuous manner. This is most likely due to the design approach for the outermost fuselage profile, which is extended longitudinally to the end of the propeller connection in the center of the fuselage. This can be seen in Figure 3.5. The extension is designed with a tangential line. A better approach would be a curvature continuous spline. Furthermore, the design of the wing with the actual wing root profile might lead to other aerodynamic results since it is more reflexed than the outermost profile of the fuselage.

The required cross-section for the numerical analysis at $Y = 664$ mm results from the design of the wing. The geometry deviation from the 3D scan is small, although the control surface is modeled together with the rest of the profile. A curvature analysis proves a minimum continuity of G2.

5.2 Numerical Results

Clean airfoil performance
The deviation in the drag- and pitch moment coefficients between XFLR5 and FENSAP for the clean S5010 airfoil can be explained with the pressure distribution shown in Figure 4.6. The main difference is that, compared to FENSAP, XFLR5 predicts an earlier transition from laminar to turbulent. This means that in the range from approximately $x/c = 0.55$ to $x/c = 0.62$, FENSAP calculates a more negative pressure coefficient on the suction side of the profile. In the range of approximately $x/c = 0.9$, where the reflex effect of the profile is noticeable, the pressure coefficient is also lower than in the XFLR5 pressure distribution, but this time in the positive range. Both effects lead to a decreased pitching-up moment for the FENSAP solution in comparison to the XFLR5 solution. This is confirmed in Figure 4.5. The lower drag of the higher Reynolds number is to a reduced skin friction drag [35].

Ice shapes and their aerodynamic effects
As shown in Figure 4.8, the MCCS and the local section show significant differences, especially for the glaze ice case. This is due to the fact that occurring droplets do not freeze immediately and can migrate further downstream. This is known as runback water and can lead to 3D effects. The difference in the MCCS and the local ice shapes is less pronounced for the rime ice case since the ice freezes immediately and no runback water occurs. The numerical results of the ice shapes show generally less ice accumulation compared to the IWT tests. The pronounced feathers in the rime ice case are not shown in the calculated ice shapes. This could be due to a grid resolution that is too low to resolve these structures. The mixed ice case shows substantial deviations in the ice shape from the IWT results. With the selected settings, the constant density model shows a significantly too small amount of ice and a deepening in the area of the stagnation point that does not correspond to IWT results. The upper surface appears more like a rime ice geometry, and 3D effects are not captured. This leads to significantly better aerodynamic performance regarding lift, drag, and stall angle than the IWT ice shape,which is shown in Figure 4.12. Another uncertainty regarding the deviation between the calculated ice shapes and the measured geometry is the swept-back wing of the Skywalker X8. The resulting 3D effects cannot be modeled in the 2D simulation at the wing section.

6 Conclusion

The first objective of this work is to create a CAD- model of the Skywalker X8 that can be used for future 3D CFD-simulations. In addition, the previously unknown wing profile of this UAV should be derived from this design. For this purpose, the UAV is reverse-engineered based on a publically available 3D scan and on an existing wing, which is cut at different positions. The profile sections of the cut wing are scanned on a conventional printer and used as validation for the correct scaling of the 3D model. The combination of the 3D scan and 2D profile section scans are used to create a wing model with winglets and a fuselage model. The goal is an aerodynamically smooth surface. Therefore, a G2-continuous curvature distribution of the surface and the profile sections is aimed at. For the airfoil sections, this is achieved by using 7^{th}-order B-splines that are well-controllable. Generally, the surface can be created with a continuous curvature. However, due to the design method and the complex geometry of the Skywalker X8, this cannot be achieved at some transition points. A possible improvement in the rear fuselage area is discussed in section 5.1. Multiple surface deviation, surface curvature, and profile curvature analyses were performed to obtain the best possible match between the 3D and 2D scans and the reconstructed surfaces. Based on the reverse-engineered surface, a well-matching airfoil at the relevant span-wise position $Y = 664$ mm is found.

The second objective is the numerical analysis of the performance loss due to ice accretion on the X8-664 profile. Since this profile is unknown, no aerodynamic test data regarding lift-drag- and pitch moment are available. Therefore, the numerical setup of the clean airfoil performance model and a grid convergence study have been performed with the comparable S5010 reference airfoil. The resulting parameters are later used with the X8-664 airfoil. The ice accretion on the Skywalker X8-664 airfoil has been analyzed at three different temperatures for glaze ice, mixed ice, and rime ice according to previously conducted IWT tests. The ice shapes, which are calculated in the simulation, are then compared with the digitized ice shapes from the IWT test. For this purpose, the MCCS and the local section in the span direction at $Y = 664$ are used. The MCCS is the envelope curve from several sections parallel to the reference section. A large deviation between the local cut and the MCCS appears in the glaze ice case. In that case, the impinging droplets do not freeze immediately and can migrate further downstream. This can lead to significant 3D effects and change the shape of the MCCS depending on the number and the position of the cuts. Therefore, further research is required to determine whether the MCCS is a suitable method for comparison with CFD ice shapes where significant 3D effects are expected to occur.

Regarding the calculated ice shapes in the ice accretion simulation, it is shown that the accumulated ice mass is generally too low. Especially the ice shape in the mixed ice regime, in combination with the constant density model, shows significant differences to both the local cut and the MCCS. This also represented in much less aerodynamic penalties compared to the impact density model and the MCCS. It is interesting to note that despite the different shapes, the aerodynamic performance of the impact ice model differs only slightly from the IWT results and shows the correct trend. However, this must be validated using further examples regarding both the simulation of the MCCS geometry and the calculated ice shape. It should also be noted that the impact density ice model in FENSAP-ICE 2023 R2 is only a beta feature, and therefore, no optimal results can yet be obtained. Furthermore, the numerical investigation of the digitized measured ice shapes represents an interesting possibility to compare the aerodynamic performance loss of calculated ice shapes to measured ice shapes. However, as mentioned before, the MCCS and the aerodynamic performance might vary due to 3D effects, the number of cuts, and their position. Furthermore, no grid-dependence study has been performed for the MCCS ice shapes. Since the geometry is complex with sharp corners, it might be challenging to find an efficient but adequate mesh to discretize the ice shape. Furthermore, no surface roughness model was used in this work. Regarding the aerodynamic performance loss, it is generally seen that the ice shapes measured in the IWT tests show a more significant increase in drag than the calculated ice shapes. Furthermore, the stall angle in the mixed- and rime ice case is usually overestimated, which is considered highly severe because stalling the UAV based on a poor stall angle prediction might lead to a loss of the aircraft.

It is assumed that the difference in aerodynamic performance is mainly due to the lack of ice mass. Therefore, an approach for future projects might be to extend the icing time until the calculated ice shape correlates with the IWT test geometries. Furthermore, test data regarding the aerodynamic performance of iced profiles would be extremely helpful in validating the numerical calculation of the MCCS ice shapes. The development of a measurement system that still delivers good results under icing conditions would be an exciting project.

Bibliography

[1] Hann, Richard ; Johansen, Tor A.: *Unsettled Topics in Unmanned Aerial Vehicle Icing*. In: *SEA International* , 2020. – ISBN 978-1-4686-0169-5

[2] Hann, Richard: *Atmospheric Ice Accretions, Aerodynamic Icing Penalties, and Ice Protection Systems on Unmanned Aerial Vehicles*, NTNU Trondheim, Dissertation, July 2020

[3] : *Federal Aviation Administration: FAA AEROSPACE FORECAST Fiscal Year 2022-2042*. 2022

[4] : *Federal Aviation Administration: FAA AEROSPACE FORECAST Fiscal Year 2020-2040*. 2020

[5] Mohsan, Syed Agha H. ; Othman, Nawaf Qasem H. ; Li, Yanlong ; Alsharif, Mohammed H. ; Khan, Muhammad A.: *Unmanned aerial vehicles (UAVs): practical aspects, applications, open challenges, security issues, and future trends*. In: *Intelligent Service Robotics* , 2023, January. – ISSN 1861-2784. – DOI 10.1007/s11370-022-00452-4

[6] Airelectronics: *X8 Flying Wing*. – URL `www.airelectronics.esinfo@airelectronics.es`. – Access date: 2023-10-20

[7] Schwarze, Rüdiger: *CFD-Modellierung*. Springer Berlin Heidelberg, 2013. – ISBN 9783642243783. – DOI 10.1007/978-3-642-24378-3

[8] Organization, International Civil A.: *ICAO Cir 328, Unmanned Aircraft Systems (UAS)*. 2011

[9] Kim Lynge Sørensen, Richard Hann Ben C. Bernstein Morten H.: *UAV ATMOSPHERICICING LIMITATIONS*. , 2021, May

[10] Bragg, M. B. ; Broeren, A. P. ; Blumenthal, L. A.: *Iced-airfoil aerodynamics*. In: *Progress in Aerospace Sciences* 41, 2005, S. 323–362. – ISSN 03760421. – DOI 10.1016/j.paerosci.2005.07.001

[11] Gerlinger, Peter: *Numerische Verbrennungssimulation*. Springer, 2005. – 400 S. – ISBN 9783540233374. – DOI 10.1007/978-3-540-27535-0

[12] Blazek, Jiri: *COMPUTATIONAL FLUID DYNAMICS:PRINCIPLES AND APPLICATIONS*. Elsevier Science, 2001. – 460 S. – ISBN 9780080430096

[13] Schlichting, H. ; Gersten, K. ; Krause, E. ; Oertel, H. J.: *Grenzschicht-Theorie*. Springer, 2006. – 799 S. – ISBN 9783540230045

[14] Liu, Fangqing: *A Thorough Description Of How Wall Functions Are Implemented In OpenFOAM.* , 2017

[15] *Siemens Simcenter STAR-CCM+ User Guide*. 14.04.013-R8

[16] Ghaib, Karim: *Einführung in die numerische Strömungsmechanik*. Springer Vieweg, 2019. – ISBN 9783658269227. – DOI 10.1007/978-3-658-26923-4

[17] Arvidson, Sebastian: *Methodologies for RANS-LESinterfaces in turbulence-resolvingsimulations*, Chalmers University of Technology Gotheburg, Dissertation, 2017

[18] SPALART, P. ; ALLMARAS, S.: *A one-equation turbulence model for aerodynamic flows.* , 1992, January. – DOI 10.2514/6.1992-439

[19] P. G. Huang, T. J. C.: *Assessment of ClosureCoefficients for Compressible-Flow Turbulence Models.* , 1992

[20] Menter, F. R.: *Two-equation eddy-viscosity turbulence models for engineering applications*. In: *AIAA Journal* 32, 1994, August, Nr. 8, S. 1598–1605. – ISSN 1533-385X. – DOI 10.2514/3.12149

[21] ANSYS, Inc.: *Ansys FENSAP-ICE User Manual*, July 2023

[22] Bourgault, Yves ; Boutanios, Ziad ; Habashi, Wagdi G.: *Three-Dimensional Eulerian Approach to Droplet Impingement Simulation Using FENSAP-ICE, Part 1: Model, Algorithm, and Validation*. In: *Journal of Aircraft* 37, 2000, January, Nr. 1, S. 95–103. – ISSN 1533-3868. – DOI 10.2514/2.2566

[23] Beaugendre, Héloïse ; Morency, François ; Habashi, Wagdi G.: *Development of a Second Generation In-Flight Icing Simulation Code*. In: *Journal of Fluids Engineering* 128, 2006, Nr. 2, S. 378–387. – DOI 10.1115/1.2169807

[24] Peter Stephan, Matthias Kind Dieter Mewes Karlheinz Schaber Thomas W. (Publisher:): *VDI-Wärmeatlas: Fachlicher Träger VDI-Gesellschaft Verfahrenstechnik und Chemieingenieurwesen*. Springer Berlin Heidelberg, 2019. – ISBN 9783662529898. – DOI 10.1007/978-3-662-52989-8

[25] MESSINGER, BERNARD L.: *Equilibrium Temperature of an UnheatedIcing Surface as a Function of A i r Speed*. In: *Journal of the Aeronautical Sciences* 3, 1936, July, Nr. 9, S. 322–325. – ISSN 1936-9956. – DOI 10.2514/8.252

[26] Habashi, Héloïse Beaugendre; Francois Morency; Wagdi G.: *FENSAP-ICE's Three-Dimensional In-Flight Ice Accretion Module*. In: *JOURNAL OF AIRCRAFT* 40, 2003, April, Nr. 2. – ISSN 0021–8669. – DOI 10.2514/2.3113

[27] Morency, Héloïse ; Baruzzi Guido ; Habashi W.: *FENSAP-ICE - A comprehensive 3D simulation system for in-flight icing.* , 2001

[28] Roache, Patrick J. ; Ghia, Kirti N. ; White, Frank M.: *Editorial Policy Statement on the Control of Numerical Accuracy.* In: *Journal of Fluids Engineering* 108, 1986, March, Nr. 1, S. 2. – ISSN 1528-901X. – DOI 10.1115/1.3242537

[29] : *Examining Spatial (Grid) Convergence.* – URL `https://www.grc.nasa.gov/WWW/wind/valid/tutorial/spatconv.html`. – Access date: 2024-02-29

[30] : *DIY DRONES.* – URL `https://diydrones.com/profiles/blogs/x8-3d-scanning`. – Access date: 2024-04-03

[31] Selig, Michael S. ; Guglielmo, James J. ; Broeren, Andy P. ; Giguere, Philippe: *Summary of Low-Speed Airfoil Data - Vol. 2.* SoarTech Publications, April 1996. – ISBN 9780964674721

[32] Westoby, M.J. ; Brasington, J. ; Glasser, N.F. ; Hambrey, M.J. ; Reynolds, J.M.: *'Structure-from-Motion' photogrammetry: A low-cost, effective tool for geoscience applications.* In: *Geomorphology* 179, 2012, December, S. 300–314. – ISSN 0169-555X. – DOI 10.1016/j.geomorph.2012.08.021

[33] Sam Lee, Mark P.: *Comparison of Ice Shapes on Full-Chord and Truncated Swept Wing Models.* , 2021

[34] : *T-Rex Tab.* – URL `https://www.pointwise.com/doc/user-manual/grid/solve/unstructured-domains/t-rex.html`. – Access date: 2024-04-09

[35] Gudmundsson, Snorri: *Aircraft Drag Analysis.* Elsevier, 2014. – 661–760 S. – DOI 10.1016/b978-0-12-397308-5.00015-5